This is the peer-reviewed, final accepted version for American Mineralogist, published by the Mineralogical Society of America.
The published version is subject to change. Cite as Authors (Year) Title. American Mineralogist, in press.
DOI: https://doi.org/10.2138/am-2021-7268. http://www.minsocam.org/

Revision 3

Ab initio study of structural, elastic and thermodynamic properties of Fe_3S at high pressure: implications for planetary cores

Karen Valencia[a], Aldemar De Moya[a,b], Guillaume Morard[c,d] , Neil L. Allan[e] and Carlos Pinilla[a,e]

[a] *Departamento de Física y Geociencias, Universidad del Norte, Km 5 Via Puerto Colombia, Barranquilla, Colombia*

[b] *Departamento de Ciencias Naturales y Exactas, Universidad de la Costa, Calle 58 No. 55-66, Barranquilla, Colombia*

[c] *Sorbonne Université, Institut de Minéralogie, de Physique des Matériaux, et de Cosmochimie (IMPMC), UMR CNRS 7590, IRD, Muséum National d'Histoire Naturelle, Paris, France.*

[d] *Now at: Université Grenoble Alpes, CNRS, ISTerre, F-38000 Grenoble*

[e] *School of Chemistry, University of Bristol, Cantock's Close, BS8 1TS, Bristol, United Kingdom*

ABSTRACT

Using density functional theory electronic structure calculations, the equation of state, thermodynamic and elastic properties and sound wave velocities of Fe_3S at pressures up to 250 GPa have been determined. Fe_3S is found to be ferromagnetic at ambient conditions but becomes non-magnetic at pressures above 50 GPa. This magnetic transition changes the *c*/*a* ratio leading to a more isotropic compressibility, and discontinuities in elastic constants and isotropic sound velocities. Thermal expansion, heat capacity and Grüneisen parameters are calculated at high pressures and elevated temperatures using the quasiharmonic approximation. We estimate Fe-Fe and Fe-S force constants, which vary with Fe environment, as well as the $^{56}Fe/^{54}Fe$ equilibrium reduced partition function in Fe_3S and compare these results with recently reported experimental values. Finally, our calculations under the conditions of the Earth's inner core allow us to estimate a S content of 2.7 wt%S, assuming the only components of the inner core are Fe and Fe_3S, a linear variation of elastic properties between end-members Fe and Fe_3S and that Fe_3S is kinetically stable. Possible consequences for the core-mantle boundary of Mars are also discussed.

This is the peer-reviewed, final accepted version for American Mineralogist, published by the Mineralogical Society of America.
The published version is subject to change. Cite as Authors (Year) Title. American Mineralogist, in press.
DOI: https://doi.org/10.2138/am-2021-7268. http://www.minsocam.org/

ARTICLE INFO

Keywords:
Fe_3S
First-principles calculations
High pressure
Thermodynamic properties

INTRODUCTION

The Earth's core is composed of iron (Fe) alloyed with Ni (~5wt%) and lighter elements which account for a density deficit compared to pure Fe (~10 % for the liquid outer core and ~3% for the solid inner core) (Poirier, 1994). The list of possible light element candidates in the outer core include S, Si, O, C, and H (Hirose et al. 2013; Litasov and Shatski, 2016). Sulfur is a promising candidate because of its high abundance in iron meteorites (Chabot 2004), and its compatibility with the liquid outer-core density (Haijun et al., 2013; Morard et al., 2013) but it is also considered too volatile to be the major light element in the core, a constraint which imposes a limit of ~2 wt% on the maximum S content (Dreibus and Palme, 1996; McDonough, 2003). However, a recent geochemical study has revised this value to 6 wt%, potentially making S a major light element in the core (Mahan et al., 2017). To rationalise geophysical observation and to constrain the S concentration in the Earth's core, a detailed understanding from experiment and theory of the physical properties of compounds in the Fe-S binary system under extreme pressure is needed.

Many experimental studies have been used to study the stability and physical properties of the solid and liquid phases in the Fe-FeS binary system under conditions of planetary interiors (Li et al., 2001; Ono and Kikegawa, 2006; Chen et al., 2007; Morard et al., 2008; Kamada et al., 2012; Kamada et al.,

2014). In the Fe-S phase diagram, the intermediate compound Fe_3S is stable from 21 GPa (Fei et al. 2000) up to approximately 250 GPa (Ozawa et al., 2013). Above this pressure, Fe_3S decomposes into Fe_2S-B2 and Fe-HCP. Mössbauer spectroscopy (Lin et al. 2004) shows that a magnetic collapse occurs in Fe_3S at 21 GPa. In addition, using synchrotron x-ray diffraction and laser-heated diamond–anvil cells, the solubility of S in the eutectic melt has been measured at pressures from 34 GPa to 254 GPa (Mori et al., 2017).

It is now possible to use *ab initio* quantum mechanical methods, usually based on periodic density functional theory (DFT), to study the behaviour of compounds under the high pressures and elevated temperatures of the Earth's core, allowing detailed examination of the physical, mechanical and chemical properties of these materials and complementing experimental studies (Alfe et al., 2000; Belonoshko et al., 2000; Alfè et al., 2002b; Belonoshko and Ahuja, 2003; Gavryushkin et al., 2016). In this work we study the behaviour of crystalline Fe_3S structures under pressure using such methods, considering the two most stable polymorphs: a face-centred cubic ($AuCu_3$-type) structure with $Pm\bar{3}m$ symmetry, with one formula unit per primitive unit cell (Sherman, 1997) and the experimentally observed tetragonal (Fe_3P-type) structure with $I\bar{4}$ symmetry, with eight formula units per primitive unit cell (Fei et al., 2000; Martin et al., 2004). We determine, as a function of pressure and temperature, the structural and dynamical stability of these two structures shown in Figure 1. We estimate properties such as thermal expansion coefficients, force constants and sound velocities as a function of pressure and temperature. Such datasets can be used as a toolbox for modelling planetary-cores dynamics and formation processes (Alfe et al., 2000; Aurnou, 2007; Alboussière et al., 2010; Adams et al., 2015; Wicht and Sanchez, 2019).

This is the peer-reviewed, final accepted version for American Mineralogist, published by the Mineralogical Society of America.
The published version is subject to change. Cite as Authors (Year) Title. American Mineralogist, in press.
DOI: https://doi.org/10.2138/am-2021-7268. http://www.minsocam.org/

METHODS

Density functional theory (DFT) calculations were carried out using the Vienna *ab-initio* simulation package (VASP) (Kresse and Furthmüller, 1996), which expands the electronic wavefunction on a plane wave basis set and incorporates the projected augmented wave (PAW) method for pseudopotentials (Kresse and Joubert, 1999). The energy of electronic exchange and correlation was calculated using the generalized gradient approximation by the Perdew-Burke-Ernzerhof revised for solids (PBEsol) (Perdew et al., 1996; Perdew et al., 2008).

Martin et al. (2004) have previously performed first-principles calculations on the two polymorphs of Fe_3S we consider here (Figure 1), but the authors took no explicit account of magnetic effects. We have carried out calculations both spin-unrestricted (high spin, ferromagnetic) where atoms are allowed to have a net magnetic moment and also spin-restricted where the net magnetic moment is constrained to be zero (low spin). Several studies on transition metal compounds have pointed out that the GGA approximation often yields unsatisfactory results for highly correlated systems. Thus in addition to GGA calculations, we have also tested the GGA+U method using the formulation of Dudarev et al. (1998) with several U_{eff} parameters ranging from 0 to 4.0 eV in order to select the value that reproduces best the static and magnetic properties of Fe_3S. However, most of these calculations with a non-zero U_{eff} predict a total magnetic moment for this system at pressures over 100 GPa in disagreement with experiment. In particular, we have tested a value of U_{eff} of 1.7 eV, similar to the one suggested by Devey et al. (2009) for other FeS alloys and found using the method of Cococcioni and de Gironcoli (2005). However, the calculated bulk modulus of the tetragonal phase of Fe_3S with GGA+U is 20% larger than even the largest experimental value in Table 1. Thus, from the available choices, we have selected the GGA method, which has been shown to yield good results for other Fe alloys (Mookherjee, 2011; Wu et al., 2011; Gu et al., 2014).

This is the peer-reviewed, final accepted version for American Mineralogist, published by the Mineralogical Society of America.
The published version is subject to change. Cite as Authors (Year) Title. American Mineralogist, in press.
DOI: https://doi.org/10.2138/am-2021-7268. http://www.minsocam.org/

We have chosen PAW pseudopotentials for Fe with electron configuration [Ne] $3s^2$ $4s^1$ $3p^6$ $3d^7$, while for S we used a [Ne] $3s^2$ $3p^4$ configuration. Calculations were performed using an energy cutoff of 600 eV (tested for convergence) and *k*-point grids were sampled ranging from 4 × 4 × 4 to 11 × 11 × 11 to test for total energy and force convergence with respect to grid size. We found the total energy to be converged within 0.01 eV/formula unit for the tetragonal and $AuCu_3$-type phases of Fe_3S using 4 × 4 × 4 and 10 × 10 × 10 mesh grids, both centred on the gamma point, respectively.

To understand the dynamical stability of these structures we have examined the vibrational properties. Phonon frequencies and thermodynamic properties were calculated using the frozen-phonon approach as implemented in the PHONOPY code (Togo and Tanaka, 2015). All atoms not equivalent by symmetry operations were displaced by 0.01 Å in a 2x1x2 supercell to obtain the forces in the perturbed system and then used to construct the force constant matrix. Phonon frequencies are given by the eigenvalues of the dynamical matrix. We found convergence for all calculated thermodynamic properties using a 4x4x4 reciprocal *q*-space mesh. We calculate free energies and heat capacities as a function of temperature and subsequently force constants and the equilibrium reduced partition function for $^{56}Fe/^{54}Fe$ in the solid phases of Fe_3S and Fe. These results are compared with those recently obtained experimentally by Liu et al. (2017).

RESULTS

Structural properties and equation of state

Fig. 2 shows the calculated energy vs. volume curves for the magnetic and non-magnetic solutions for the cubic and tetragonal phases. At all studied volumes the tetragonal phase has a lower internal energy than the cubic. At small volumes the difference in energy between the ferromagnetic and non-

magnetic solutions is small, but at larger volumes above 38 Å^3/formula unit the ferromagnetic solution is appreciably lower than the non-magnetic. The results for the tetragonal ferromagnetic phase in Figure 2 were fitted to a third order Birch-Murnaghan equation giving static values of V_0 = 339.0 Å^3, K_0 = 175 GPa and K'_0 = 5.1. Note that V_0 here is not the volume per formula unit but the volume per (tetragonal) unit cell which contains eight formula units. The calculated value of V_0, the volume at zero pressure is about 11% less than the room temperature experimental data summarised in Table 1 (Fei et al., 2000; Seagle et al., 2006; Chen et al., 2007; Kamada et al., 2014). Comparison with the values of Martin et al. (2004) is less straightforward since their calculations are non-magnetic; our calculations suggest that V_0 for the non-magnetic state is about 6% smaller than that for the magnetic, which is consistent with the conclusions of Vocadlo et al. (2002) and Ono and Mibe (2010) for Fe_3C.

The calculated bulk modulus, K_0, is 5 GPa higher than the largest experimental value (Fei et al., 2000) and is in reasonable agreement with all the experimental values as shown in Table 1. It it is worth noting a large variation in the experimental K_0 from 119 GPa to 170 GPa. The value of K'_0, the first derivative of the bulk modulus, agrees with two of the larger values reported (Chen et al., 2007; Kamada et al., 2014). Overall agreement with experiment for V_0 and K_0 improves somewhat when zero point contributions and finite temperature corrections are included, as we show later.

The calculated magnetic moments of the three Fe in tetragonal Fe_3S at zero pressure are 2.12 μ_B, 1.40 μ_B and 1.82 μ_B for FeI, FeII and FeIII, respectively (see Fig. 3). All three magnetic moments decrease with increasing pressure, albeit at different rates and are predicted to go to zero at approximately 80 GPa. The variation with pressure for all three sites is very similar to those in calculations reported for the $I\bar{4}$ phase of Fe_3P (Gu et al., 2014). The calculated values are broadly consistent with values of 1.8μ_B and 1.1μ_B which we have estimated following Dubiel (2009) from the results of experimental synchrotron Mossbauer spectroscopy at zero pressure (Lin et al. (2004)). The experimental values are

averages of only two magnetic hyperfine field sites derived from time spectra. This overestimation of the magnetic moment has been observed in previous first principles calculations for Fe_3C and Fe_3P, which adopt similar structures (Vocadlo et al., 2002; Gu et al., 2014). Temperature which affects the magnetic behaviour of materials due to atomic thermal vibrations that oppose the coupling forces between adjacent atomic dipoles, is not included in the calculations reported in Figure 3. Thus our calculated magnetic moments are expected to be overestimates.

The calculated average magnetic moment halves from $1.5\mu_B$ to $0.7\mu_B$ between 20-50 GPa. For comparison, Shen et al. (2003) report a magnetic transition at 20-25 GPa using X-ray emission spectroscopy and Lin et al. (2004) a magnetic collapse at 21 GPa from time spectra of synchrotron Mössbauer spectroscopy. The calculated pressure at which the magnetic moments are close to zero is much higher than these experimentally reported pressures but, nevertheless, a broad range for the calculated transition is consistent with different behaviour with pressure of the three Fe in different environments in the unit cell, and with comparable calculations for Fe_3C (e.g., Ono and Mibe (2010), for Fe_3P (Gu et al. (2014)) and recent experiments on Fe_3P (Lai et al., 2020). The calculated transition pressure in Fe_3P (Gu et al., 2014) is also considerably higher than the reported pressure.

The variation of the *c*/*a* ratio of the tetragonal phase (Fig. 4) with pressure from the spin unrestricted calculations changes markedly around 50 GPa, consistent with the experimental values of (Kamada et al., 2014). Our values for *c/a* at pressures above 50 GPa are around 2% lower than those reported experimentally at room temperature by Seagle et al. (2006) and Kamada et al. (2014). There is considerable scatter in the experimental values which hinders comparison of experiment and theory, but both suggest that after the magnetic transition above 75 GPa the structure compresses almost isotropically. Previous experimental studies on similar compounds such as Fe_3P, have shown that in the magnetic state the magnetic moments are aligned mainly in the *ab*-plane, with contributions along the *c* direction close to zero (Liu et al., 1998; Liu et al., 2003). In the non-magnetic state the magnetic

174 moments in the *ab*-plane are lost and the compressibility along the *a*-axis increases. Comparable
175 behaviour has been seen in Fe_3P by Gu et al. (2016). It is tempting to associate the complex variation
176 of *c/a* in Fig. 4 between 50 GPa and 75 GPa to differences in the magnitudes of the magnetic
177 interactions of the three nonequivalent iron sites (as also seen in Fig. 3).

178 **Dynamical stability and thermal properties**

179 In order to take into account the dependence of volume and energy on temperature, we use the
180 quasiharmonic approximation (QHA), in which phonon frequencies are a function of volume but not
181 of temperature, to calculate the Helmholtz free energy (*A*):

182 $$A(V,T) = U_0(V) + \frac{1}{2}\sum_{\boldsymbol{q},i} h\nu_i(\boldsymbol{q},V) + k_B T \sum_{\boldsymbol{q},i} \ln\left[1 - e^{-h\nu_i(\boldsymbol{q},V)/k_B T}\right] \quad (1)$$

183 The first, second and third terms are the static, zero point and vibrational contributions to the free
184 energy respectively, the ν_i are the frequencies of vibrational modes with wavevector **q**, *h* Planck's
185 constant and k_B Boltzmann's constant. The summation is performed over a 4x4x4 regular mesh in
186 reciprocal space using a 1x1x2 supercell which is sufficiently large to lead to convergence of the
187 vibrational frequencies to 0.01 cm^{-1}. Anharmonic effects become important at larger volumes and
188 eventually the QHA fails. High pressures correspond to smaller volumes, so the quasiharmonic
189 approximation usually works well over a large range of temperatures at elevated pressures (Allan et
190 al., 1991; Allan et al., 1993).
191 In order to compare with experiment we have estimated the volumetric thermal expansion of
192 tetragonal Fe_3S within the quasiharmonic approximation as a function of pressure, at temperatures
193 for which there are experimental data (300-900 K). Calculation of the anisotropic thermal expansion
194 requires determining the equilibrium structure at pressure *P* and temperature *T* by means of a full
195 minimisation of the (non-equilibrium) Gibbs energy (*A*+*PV*) with respect to the lattice parameters *a*
196 and *c* and the basis atom positions (Taylor et al., 1997; Taylor et al., 1998) at each pressure and

197 temperature: this is too computationally expensive. Thus we have used what has been recently
198 referred to as the "statically-constrained" quasiharmonic approximation (Allan et al., 1996; Carrier et
199 al., 2007; Otero-de-la-Rosa et al., 2011). The calculated volumetric thermal expansion coefficient is
200 shown as a function of temperature for pressures of 50 GPa and above in Figure 5; all the curves in
201 this and subsequent figures are for the non-magnetic solution at 50 GPa; the spin-unrestricted results
202 are very similar. At a given pressure the variation of α with temperature is approximately linear at
203 higher temperatures. At a given temperature α decreases rapidly with pressure. At the very highest
204 volumes and temperatures (corresponding to pressures under 20 GPa at high temperatures above 1000
205 K) calculated expansion coefficients are unphysically high due probably to the breakdown of the
206 quasiharmonic approximation at large internuclear separations (Allan et al., 1991; Allan et al., 1993)
207 and so are not plotted. At very high pressures α only increases slowly with increasing temperature.
208
209 The variation of volume with pressure for tetragonal Fe_3S (tetragonal phase) at different temperatures
210 is plotted in Figure 6. The inclusion of vibrational terms improves the agreement between theory and
211 experiment - the volume at 0 GPa (V_0) and 300 K extrapolated from our calculations at 50 GPa – 200
212 GPa is 3% larger than the static value and the isothermal bulk modulus decreases by 5%, with K'_0
213 almost unchanged (Table 1). Nevertheless, the calculated volume is still underestimated by 8%; the
214 PBEsol functional often underestimates the equilibrium volume of metal and metal alloys.
215
216 The dynamical stability of the tetragonal phase of Fe_3S was studied over a wide pressure range from
217 0 (magnetic) to 350 GPa (non-magnetic) by examination of the calculated phonon dispersion curves.
218 Dispersion curves for 0 and 50 GPa are shown in Figure 5. Imaginary frequencies are present at 0
219 GPa; only above 50 GPa does the structure become dynamically stable. We have performed phonon

This is the peer-reviewed, final accepted version for American Mineralogist, published by the Mineralogical Society of America.
The published version is subject to change. Cite as Authors (Year) Title. American Mineralogist, in press.
DOI: https://doi.org/10.2138/am-2021-7268. http://www.minsocam.org/

frequency calculations at pressures up to 350 GPa, values relevant to the inner core, and the $I\overline{4}$ phase is dynamically stable up to this pressure.

Dynamic stability does not guarantee thermodynamic stability. Recently, it has been suggested that Fe3S can decompose into pure Fe-HCP and a B2-type Fe_2S structure above 250 GPa (Tateno et al., 2019; Thompson et al., 2020). The thermodynamic stability of Fe_3S is determined by the free energy for the reaction:

$$Fe_3S = Fe^{(hcp)} + Fe_2S^{(B2)}$$

Our calculated enthalpy in the static limit for this decomposition at 50 GPa is -0.5 eV. The enthalpy of reaction decreases with pressure and at inner core conditions of 350 GPa is -1.25 eV. The negative value shows that although Fe_3S is dynamically stable at 50 GPa, it is thermodynamically unstable with respect to decomposition into Fe-HCP and Fe_2S-B2 even at pressures well below 250 GPa. Nevertheless, experiment shows Fe_3S is stable at least to 200 GPa (Kamada et al., 2012; Kamada et al., 2014). Ozawa et al. (2013) only observed decomposition of Fe_3S into two phases at 271 GPa and 2530 Km. At the low pressure end, Fei et al. (2000) established the existence of Fe_3S at 21 GPa at temperatures between 1220 K and 1673 K. Overall, observation of Fe_3S well beyond the calculated range of thermodynamic stability suggests a substantial barrier to decomposition over a wider range of high pressures at which Fe_3S is kinetically stable.

The calculated temperature variation of the dimensionless thermal Grüneisen parameter, γ_{th} ($=\alpha K_T/C_V\rho$), widely used in approximate equations of state (Barron and White, 1999) is shown at different pressures in Figure 8. At 50 GPa this varies by only approximately 2% over 0-1500 K, and the variation with temperature at higher pressures even smaller. The logarithmic isothermal volume derivative of the Grüneisen parameter, q ($= \partial \ln \gamma_{th}/\partial \ln V)_T$, is only weakly dependent on the pressure,

244 which is a common assumption made in the reduction of experimental data (Roberts and Ruppin,
245 1971).

246

247 Heat capacities at constant pressure and volume is plotted as a function of temperature in Figure 9.
248 The constant pressure heat capacity is calculated using the relationship $C_P = C_V (1+\alpha\gamma_{th}T)$, with C_V
249 determined at the appropriate volume at the temperature and pressure of interest, determined from
250 the calculated thermal expansion in figure 5. Our calculated value of C_V of 562 J mol^{-1} K^{-1} at 50 GPa
251 and ambient temperature compares with a value of 620 J mol^{-1} K^{-1} estimated from inelastic neutron
252 scattering measurements by Lin et al. (2004).

253 The increase in frequencies at high pressure is related to changes in the force constants of the Fe-Fe
254 and Fe-S bonds, which increase as the bonds become stiffer. Fig. 10 shows the calculated force
255 constants taken from the dynamical matrix for the three types of Fe atoms in the $I\overline{4}$ structure as a
256 function of pressure. Our results are in good agreement with experimental data from NRIXS reported
257 by Lin et al. (2004) and Liu et al. (2017), as shown in Fig. 10. A particular advantage of our
258 calculations is that, while experiment measures only an average force constant, we can assess the
259 variation of the force constants with local structural environment. The force constant for a FeI bond
260 is slightly lower than those involving FeII and FeIII. FeII and FeIII are bonded to three sulfur atoms
261 whereas FeI is bonded only to two, so the effective charge on the FeI atom is lower. This difference
262 in bonding environment leads to small differences in quantities such as the $^{56}Fe/^{54}Fe$ isotope
263 fractionation factor. The equilibrium reduced partition function (β-factor) that describes the isotopic
264 fractionation properties between a given condensed phase *a* and an ideal gas can be estimated within
265 the quasiharmonic approximation using the expression (Pinilla et al., 2015):

266

This is the peer-reviewed, final accepted version for American Mineralogist, published by the Mineralogical Society of America.
The published version is subject to change. Cite as Authors (Year) Title. American Mineralogist, in press.
DOI: https://doi.org/10.2138/am-2021-7268. http://www.minsocam.org/

$$\beta(a,Y) = \left[\prod_{i=1}^{3N_{at}} \prod_{\mathbf{q}} \frac{\nu^*_{\mathbf{q},i}}{\nu_{\mathbf{q},i}} \frac{e^{-h\nu^*_{\mathbf{q},i}/2k_BT}}{(1-e^{-h\nu^*_{\mathbf{q},i}/k_BT})} \frac{(1-e^{-h\nu_{\mathbf{q},i}/k_BT})}{e^{-h\nu_{\mathbf{q},i}/2k_BT}}\right]^{1/(NN_{\mathbf{q}})} \quad (2)$$

where the $\nu_{\mathbf{q},i}$ are the phonon frequencies with wave vector **q**. N_{at} is the number of atoms in the unit-cell and N is the number of sites occupied by atom Y in the unit-cell. The $\nu^*_{\mathbf{q},i}$ correspond to analogous frequencies of the phase containing the heavy isotope. The product in equation 2 is performed on a grid containing 6x6x6 $N_{\mathbf{q}}$ **q**-vectors to ensure convergence with respect to grid size.

Using the expression in equation 2 we have calculated the β-factor for the isotope fractionation of $^{56}Fe/^{54}Fe$ obtaining an average value of $\delta Fe^{56}_{Fe_3S}=10^3 \ln \beta(Fe_3S,Fe)$ of 9.58‰ at 50 GPa and 298 K which is in good agreement with the 10.2‰ reported by Dauphas et al. (2012). The different local environment of the three types of Fe atoms within the unit cell leads to a 1.3‰ difference in the β-factor between FeI and FeII and between FeI and FeIII which suggests that Fe_3S should be slightly richer in ^{56}Fe isotopes at the FeII and FeIII sites than at FeII.

Elastic moduli and sound wave velocities

In Figure 11a we show the elastic constants at zero temperature calculated using the strain vs stress relationship for pressures up to 250 GPa where Fe_3S is predicted to decompose into Fe-HCP and FeS-B2. For the tetragonal structure of Fe_3S there are seven independent elastic constants: C_{11}, C_{33}, C_{44}, C_{66}, C_{12}, C_{13} and C_{16} (Mouhat and Coudert, 2014). These constants have been calculated in the static limit for the magnetic state at pressures below 50 GPa and for the non-magnetic thereafter. The elastic constants increase monotonically as a function of pressure (Fig. 11a). The increase with pressure is less marked in the non-magnetic phase (i.e., above 50 GPa) than in the magnetic (i.e., below 50 GPa)

This is the peer-reviewed, final accepted version for American Mineralogist, published by the Mineralogical Society of America.
The published version is subject to change. Cite as Authors (Year) Title. American Mineralogist, in press.
DOI: https://doi.org/10.2138/am-2021-7268. http://www.minsocam.org/

with the slight exception of C_{44}, C_{66} and C_{16} perhaps related to the resistance to shear by the aligned spins in the magnetic phase. Additionally, we have used these results to estimate the isotropic longitudinal (v_P) and shear-wave (v_S) velocities for pressures up to 250 GPa (Fig. 11b):

$$v_P = \sqrt{\frac{K+\frac{4}{3}G}{\rho}} \qquad v_S = \sqrt{\frac{G}{\rho}} \qquad (3)$$

where ρ is the density of the material and K and G the bulk modulus and shear modulus as shown in Figure 11c. Our calculations include both regimes, magnetic and non magnetic. The response due to the collapse in magnetic effects can be seen from the discontinuity in the velocities around 50 GPa. Our results are in excellent agreement with those reported by (Lin et al., 2004) for pressures up to 55 GPa. The computed P- and S- wave velocities for Fe_3S are 10% larger than those found experimentally for pure Fe-HCP under the same pressure range. A linear regression of the curves in figure 11 at pressures above 100 GPa yields the equations $v_P/(\mathrm{m\ s^{-1}}) = 1.1038\rho - 1883.5$ and $v_S/(\mathrm{m\ s^{-1}}) = 0.65173\rho - 1940.5$, where the units of ρ are kg $\mathrm{m^{-3}}$.

Seismological observations indicate that the inner core is anisotropic with respect to the speed of sound (Belonoshko et al., 2008; Lincot et al., 2015; Tkalcic, 2015), with the P-waves travelling faster towards the pole than towards the equator. In order to address the pressure dependence of elastic anisotropy in Fe_3S we calculated the directional dependence of the P and S wave velocities by solving the Christoffel equation using the method implemented by Jaeken and Cottenier (2016). Using the calculated data for the full elastic tensor we see that Fe_3S exhibits a strong anisotropy in both compressional (P) and shear (S) waves (Figure 12). In particular, there is a softness for P waves along the [100] and [010] directions, and along the [110] for S waves. The effect of pressure on the anisotropic behaviour is small with the hardening of P and S waves as a function of pressure (Table 2). The loss of magnetization has an effect on the *xy* plane leading to a softening of S wave vectors.

This is the peer-reviewed, final accepted version for American Mineralogist, published by the Mineralogical Society of America.
The published version is subject to change. Cite as Authors (Year) Title. American Mineralogist, in press.
DOI: https://doi.org/10.2138/am-2021-7268. http://www.minsocam.org/

IMPLICATIONS

Using these results for Fe_3S and assuming that this phase is still stable at 350 GPa, we assume a two-component ideal solid solution in order to estimate the amount of S present in the inner core at 350 GPa. Using a similar analysis to that proposed by Badro et al. (2007), the density and compressional sound velocity can be written as

$$\rho = x\rho_1 + (1-x)\rho_2 \qquad (4)$$

and

$$v = \frac{v_1 v_2}{(1-x)v_1 + x v_2} \qquad (5)$$

where x is the volume fraction of pure HCP iron, ρ_1 (v_1) and ρ_2 (v_2) the densities (velocities) of pure Fe-HCP and Fe_3S at inner core conditions respectively. Setting $\rho = \rho_{PREM} = 12.2 \times 10^3$ kg m^{-3} and $v = v_{PREM} = 10.6 \times 10^3$ m s^{-1}, using the equation of state of pure Fe from Badro et al. (2007) ($\rho_1 = 13.2 \times 10^3$ kg m^{-3} and $v_1 = (0.94 - 1466\,\rho_1)$ m s^{-1}) and our values for v_2 as a function of density (Fig. 11b), we solve equations 4 and 5 for x and ρ_2. Thus we estimate the amount of S present in the inner core assuming Fe and Fe_3S are the only components. We find x=0.56 vol% and $\rho_2 = 10.9 \times 10^3$ kg m^{-3} leading to a sulfur content in the inner core of ≈2.7 wt%. This is similar to the maximum silicon content expected for the inner core (a maximum of 3 ±2wt.%Si) (Antonangeli et al., 2018), but is subject to the caution about the possible thermodynamic decomposition of Fe_3S discussed above into Fe-HCP and Fe_2S-B2 at high pressures and temperatures. Taking into account the calculated partitioning of sulfur between solid and liquid at ICB conditions (Alfè et al., 2002a), a value of 3.5 wt%S content in the liquid outer core is obtained. Such a sulfur content is not sufficient to account for the liquid outer core density deficit (Huang et al., 2013; Morard et al., 2013), implying the requirement of another light element more compatible with the liquid phase, such as oxygen (Alfè et al., 2002a).

In recent years Fe isotopes have been proposed as a tool to study planetary differentiation and have triggered a series of studies to investigate whether the formation of a metallic core could induce a measurable isotope fractionation between chondrites and the silica part of the Earth (Poitrasson et al., 2004; Weyer et al., 2005; Craddock and Dauphas, 2013). The results have been inconclusive so far with some studies suggesting a non-resolvable isotope difference and others finding a clear trend (Bourdon et al., 2018). Additionally, the effect of the concentration of light elements such as S, O, Si, H in the Fe fractionation between the silicate part of the mantle and a metallic core at conditions of core formation is not clear either (see for example (Poitrasson et al., 2009; Hin et al., 2012; Shahar et al., 2015)). This effect imprinted by light elements could be a signature of the density deficit in Earth's core that could lead to a way to identify the core's composition. In order to understand the effect of a light element such as S in the isotope fractionation of iron we compare the average β-factor of $^{56}Fe/^{54}Fe$ at conditions of the magma ocean (60 GPa, 3000K) calculated in this work for Fe_3S, $\delta Fe^{56}_{Fe3S} = 10^3 \ln(\beta) = 0.117‰$, with that for pure HCP iron at the same conditions $\delta Fe^{56}_{Fe} = 0.108‰$ (Pinilla et al., 2020). The difference $\delta Fe^{56}_{Fe} - \delta Fe^{56}_{Fe3S} = 0.014‰$ is an order of magnitude smaller than the findings of some authors (Shahar et al., 2015; Shahar et al., 2016) but is in better agreement with Poitrasson et al. (2009); Hin et al. (2012); Liu et al. (2017) who conclude that the addition of light elements have little effect on the iron isotope fractionation at the conditions of core formation up to concentrations of 18wt% (Bourdon et al., 2018). The small dependence of the β-factor on concentration may be related to the Fe-S bond character and coordination number.

The elastic properties of Fe_3S calculated in the present study should be valuable in the near future for the study of the core-mantle boundary (CMB) in Mars. Following the results of the Insight mission (Banerdt et al., 2019), seismic wave travel times will be available and could potentially be used to reconstruct the internal structure of Mars. The pressure at the Mars CMB is estimated at 20-25 GPa (Sohl et al., 2005), pressures at which Fe_3S is experimentally stable. Mars does not possess a magnetic

356 field, although, based on its moment of inertia and density, it is thought to have a partially liquid
357 metallic core (Yoder et al., 2003). Recent estimates of sulfur present in the core of Mars (25-35 GPa,
358 2000-2200 K) range from 7 to 17wt% due to the large partition coefficient (log $D_S^{mel\text{-}sil}$ = 2.6)
359 (Steentra and van Westrenen, 2018). Given such a large amount of S in the core, one of the first S
360 containing phases that should crystallize first is a magnetic tetragonal Fe_3S, the presence of which in
361 the core could be detected by the anisotropic seismic velocities we report in figures 11 and 12. If the
362 S content is over 15 wt% a possible top down crystallisation process could take place in the core of
363 Mars, with Fe_3S potentially present at the CMB (Breuer et al., 2015). Next seismological models of
364 the Mars interior extracted from the Insight mission could benefit from our work, potentially looking
365 for a Fe_3S layer at the Mars CMB.

366

367 We have used ab-initio computer simulation methods to study the structural, mechanical and
368 thermodynamic properties of the $I\bar{4}$ phase of Fe_3S. We have shown that this phase is the most stable
369 at high pressure and provided an equation of state for this system. We have seen a collapse in magnetic
370 order between 40-60 GPa. This magnetic transition affects the *c*/*a* ratio leading to a more isotropic
371 compressibility. Additionally, this change leads to a discontinuity in elastic constants and isotropic
372 sound velocities. The different types of Fe atoms in the structure lead to different force constants, so
373 affecting quantities such as the equilibrium isotope fractionation factor. Finally, we have presented a
374 study of thermodynamic properties and provide information on thermal expansion, heat capacity and
375 Grüneisen parameters for this structure under conditions of interest for the cores of Earth and Mars.
376 We estimate that, provided Fe_3S is kinetically stable with respect to decomposition, the inner core
377 contains approximately 2.7 wt% S.

378

ACKNOWLEDGEMENTS

This work was performed using Granado-HPC from the Universidad del Norte and SCARF from the STFC of the UK. We acknowledge funding from COLCIENCIAS and ECOSNORD through research grants No. 2015-710-51568 (Contract No. 023-2016) and grant No. FP44842-143-2017 respectively.

REFERENCES CITED

Adams, M.M., Stone, D.R., Zimmerman, D.S., and Lathrop, D.P. (2015) Liquid sodium models of the Earth's core. Progress in Earth and Planetary Science, 2, 29.

Alboussière, T., Deguen, R., and Melzani, M. (2010) Melting-induced stratification above the Earth's inner core due to convective translation. Nature, 466, 744-747.

Alfe, D., Gillan, M., and Price, G. (2000) Constraints on the composition of the Earth's core from ab initio calculations. Nature, 405, 172-5.

Alfè, D., Gillan, M.J., and Price, G.D. (2002a) Composition and temperature of the earth's core constrained by combining ab initio calculations and seismic data. Earth and Planetary Science Letters, 195, 91-98.

Alfè, D., Gillan, M.J., Vocadlo, L., Brodholt, J., Price, G.D., Trans, P., and Lond, R.S. (2002b) The ab initio simulation of the Earth ' s core Philosophical Transactions of the Royal Society A, 360, 1227-1244.

Allan, N.L., Barron, T.H.K., and Bruno, J.A.O. (1996) The zero static internal stress approximation in lattice dynamics and the calculation of isotope effects on molar volumes. Journal of Chemical Physics, 105, 8300-8303.

Allan, N.L., Braithwaite, M., Cooper, D.L., Mackrodt, W.C., and Wright, S.C. (1991) Ionic solids at high pressure and elevated temperatures: MgO (Periclase). Journal of Chemical Physics, 95, 6792.

Allan, N.L., Braithwaite, M., Cooper, D.L., Petch, B., and Mackrodt, W.C. (1993) Ionic halides and oxides at high pressure: Calculated hugoniots, isotherms and thermal pressures. Journal of Chemical Society, Faraday Transactions, 89, 4369–4374.

Antonangeli, D., Morard, G., Paolasini, L., Garbarino, G., Murphy, C.A., Edmund, E., Decremps, F., Fiquet, G., Bosak, A., Mezouar, M., and Fei, Y. (2018) Sound velocities and density measurements of solid hcp-Fe and hcp-Fe–Si (9 wt.%) alloy at high pressure: Constraints on the Si abundance in the Earth's inner core. Earth and Planetary Science Letters, 482, 446-453.

Aurnou, J.M. (2007) Planetary core dynamics and convective heat transfer scaling. Geophysical & Astrophysical Fluid Dynamics, 101, 327-345.

Badro, J., Fiquet, G., Guyot, F., Gregoryanz, E., Occelli, F., Antonangeli, D., and d'Astuto, M. (2007) Effect of light elements on the sound velocities in solid iron : Implications for the composition of Earth ' s core. Earth and Planetary Science Letters, 254, 233-238.

Banerdt, W.B., Smrekar, S., Antonangeli, D., Asmar, S., Banfield, D., Beghein, C., Bowles, N., Bozdag, E., Chi, P., Christesen, U., John, C., Gareth, C., Ingrid, D., Véronique, D., Matthew, F., Bill, F., Raphael, G., Jim, G., Domenico, G., Matt, G., John, G., Matthias, G., Jurek, G., Troy, H., Jessica, I., Catherine, J., Günter, K., Taichi, K., Sharon, K., Scott, K., Brigitte, K.-E., Mark, L., Philippe, L., Ralph, L., Justin, M., Ludovic, M., Scott, M., Chloë, M., David, M., Antoine, M., Paul, M., Nils, M.l., Seiichi, N., Claire, N., Francis, N., Mark, P., Tom, P., Ana-Catalina, P., Jose, A.R.-M., Chris, R., Nick, S., Matt, S., Aymeric, S., Tilman, S., Sabine, S., Nick, T., Jeroen, T., Nicholas, W., Renee, W., and Mark, W. (2019) Insight-the first three months on mars. 50th Lunar and planetary science conference 2019, Cont. 2132.

Barron, T.H.K., and White, G.K. (1999) Heat capacity and thermal expansion at low temperatures. 356 p. Kluwer, New York.

Belonoshko, A.B., and Ahuja, R. (2003) Stability of the body-centred-cubic phase of iron in the Earth ' s inner core. Nature, 424, 1032-1034.

Belonoshko, A.B., Ahuja, R., and Johansson, B. (2000) Quasi – Ab Initio Molecular Dynamic Study of Fe Melting. Physical Review Letters, 84, 3638.

Belonoshko, A.B., Skorodumova, N.V., Rosengren, A., and Johansson, B. (2008) Elastic anisotropy of Earth's inner core. Science, 319, 797.

Bourdon, B., Roskosz, M., and Hin, R.C. (2018) Isotope tracers of core formation. Earth-Science Reviews, 181, 61-81.

Breuer, D., Rueckriemen, T., and Spohn, T. (2015) Iron snow, crystal floats, and inner-core growth: modes of core solidification and implications for dynamis and terrestrial planets and moons. Progress in Earth and Planetary Science, 2, 39.

Carrier, P., Wentzcovitch, R., and Tsuchiya, J. (2007) First-principles prediction of crystal structures at high temperatures using the quasiharmonic approximation. Physical Review B, 76, 64116.

Chen, B., Gao, L., Funakoshi, K.-i., and Li, J. (2007) Thermal expansion of iron-rich alloys and implications for the Earth's core. Proceedings of the National Academy of Sciences of the United States of America, 104, 9162-9167.

Cococcioni, M., and de Gironcoli, S. (2005) Linear response approach to the calculation of the effective interaction parameters in the LDA+U method. Physical Review B, 71, 035105.

Craddock, P.R., and Dauphas, N. (2013) Iron isotopic composition of reference materials, geostandards and chondrites. Geostandards & Geoanalytical Research, 35, 101-123.

Dauphas, N., Roskosz, M., Alp, E.E., Golden, D.C., Sio, C.K., Tissot, F.L.H., Hu, M.Y., Zhao, J., Gao, L., and Morris, R.V. (2012) A general moment NRIXS approach to the determination of equilibrium Fe isotopic fractionation factors: Application to goethite and jarosite. Geochimica et Cosmochimica Acta, 94, 254-275.

Devey, A.J., Grau-Crespo, R., and de Leeuw, N.H. (2009) Electronic and magnetic properties of Fe_3S_4: GGA+U investigation. Physical Review B, 79, 195126.

Dreibus, G., and Palme, H. (1996) Cosmochemical constraints on the sulfur content in the Earth's core. Geochimica et Cosmochimica Acta, 60, 1125-1130.

Dubiel, S.M. (2009) Relationship between the magnetic hyperfine field and the magnetic moment. Journal of Alloys and Compounds, 488, 18-22.

Dudarev, S.L., Botton, G.A., Savrasov, S.Y., Humphreys, C.J., and Sutton, A.P. (1998) Electron-energy-loss spectra and the structural stability of nickel oxide: An LSDA+U study. Physical Review B, 57, 1505.

Fei, Y., Li, J., Bertka, C.M., and Prewitt, C.T. (2000) Structure type and bulk modulus of Fe_3S , a new iron-sulfur compound. American Mineralogist, 85, 1830-1833.

Gavryushkin, P., Popov, Z.I., Litasov, K.D., Belonoshko, A.B., and Gavryushkin, A. (2016) Stability of B2-type FeS at Earth ' s inner core pressures : Stability of B2-FeS at core pressures. Geophysical Research Letters, 43, 069374.

Gu, T., Fei, Y., Wu, X., and Qin, S. (2014) High-pressure behavior of Fe_3P and the role of phosphorus in planetary cores. Earth and Planetary Science Letters, 390, 296-303.

Gu, T., Fei, Y., Wu, X., and Quin, S. (2016) Phase stabilities and spin transitions of $Fe_3(S_{1-x}P_x)$ at high pressure and its implications in meteorites. American Mineralogist, 101, 205-210.

Haijun, H., Wu, S., Hu, X., Wang, Q., Wang, X., and Fei, Y. (2013) Shock compression of Fe-FeS Mixture up to 204 GPa. Geophysical Research Letters, 40, 687-691.

Hin, R.C., Schmidt, M.W., and Bourdon, B. (2012) Experimental evidence for the absence of iron isotope fractionation between metal and silicate liquids at 1 GPa and 1250–1300°C and its cosmochemical consequences. Geochimica et Cosmochimica Acta, 93, 164-181.

Huang, H., Wu, S., Hu, X., Wang, Q., and Wang, X. (2013) Shock compression of Fe-FeS misture up tu 204 GPa. Geophysical Research Letters, 40, 687-691.

Jaeken, J., and Cottenier, S. (2016) Solving the Christoffel equation: Phase and group velocities. Computer Physics Communications, 207, 445-451.

Kamada, S., Ohtani, E., Terasaki, H., Sakai, T., Miyahara, M., Ohishi, Y., and Hirao, N. (2012) Melting relationships in the Fe-Fe_3S system up to the outer core conditions. Earth and Planetary Science Letters, 359-360, 26-33.

Kamada, S., Ohtani, E., Terasaki, H., Sakai, T., Takahashi, S., Hirao, N., and Ohishi, Y. (2014) Equation of state of Fe_3S at room temperature up to 2megabars. Physics of the Earth and Planetary Interiors, 228, 106-113.

Kresse, G., and Furthmüller, J. (1996) Efficient iterative schemes for ab initio total-energy calculations using a plane-wave basis set. Physical Review B - Condensed Matter and Materials Physics, 54, 11169-11186.

Kresse, G., and Joubert, D. (1999) From ultrasoft pseudopotentials to the projector augmented-wave method. Physical Review B, 59, 1758.

Lai, X., Zhu, F., Liu, Y., Bi, W., Zhao, J., Alp, E.E., Hu, M.Y., Zhang, D., Tkachev, S., Manghnani, M.H., Prakapenka, V.B., and Chen, B. (2020) Elastic and magnetic properties of Fe3P up to core pressures: Phosphorus in the Earth's core. Earth and Planetary Science Letters, 531, 115974.

Li, J.Y., Fei, Y., Mao, H.K., Hirose, K., and Shieh, S.R. (2001) Sulfur in the Earth's inner core. Earth and Planetary Science Letters, 193, 509-514.

Lin, J.F., Fei, Y., Sturhahn, W., Zhao, J., Mao, H.K., and Hemley, R.J. (2004) Magnetic transition and sound velocities of Fe_3S at high pressure: Implications for Earth and planetary cores. Earth and Planetary Science Letters, 226, 33-40.

Lincot, A., Merkel, S., and Cardin, P. (2015) Is inner core seismic anisotropy a marker for plastic flow of cubic iron? Geophysical Research Letters, 42, 1326-1333.

Liu, H.-P., Andersson, Y., James, P., Satula, D., Kalska, B., Haggstrom, L., Eriksson, O., Broddefalk, A., and Nordblad, P. (2003) The antiferromagnetism of $(Fe_{1-x}Mn_x)P$, $x>0.67$ compounds. Journal of Magnetism and Magnetic Materials, 256, 117-128.

Liu, H.-P., James, P., Broddefalk, A., Andersson, Y., Granberg, P., and Eriksson, O. (1998) Structural and magnetic properties of $(Fe_{1-x}Co_x)P$ compounds: experimental and theory. Journal of Magnetism and Magnetic Materials, 189, 69-82.

Liu, J., Dauphas, N., Roskosz, M., Hu, M.Y., Yang, H., Bi, W., Zhao, J., Alp, E.E., Hu, J.Y., and Lin, J.-f. (2017) Iron isotopic fractionation between silicate mantle and metallic core at high pressure. Nature Publishing Group, 8, 1-6.

Mahan, B.M., Siebert, J., Pringle, E.A., and Moynier, F. (2017) Elemental partitioning and isotopic fractionation of Zn between metal and silicate and geochemical estimation of the S content of the Earth's core. Geochimica et Cosmochimica Acta, 196, 252-270.

Martin, P., Vocadlo, L., Alfe, D., and Price, G. (2004) An ab initio study of the relative stabilities and equations of state of Fe_3S polymorphs. Mineralogical Magazine, 65, 181-191.

McDonough, W.F. (2003) Compositional model for the Earth's core. Elsevier, New York.

Mookherjee, M. (2011) Elastic and anisotropy of Fe_3C at high pressure American Mineralogist, 96, 1530-1536.

Morard, G., Andrault, D., Guignot, N., Sanloup, C., Mezouar, M., Petitgirard, S., and Fiquet, G. (2008) In situ determination of Fe – Fe_3S phase diagram and liquid structural properties up to. Earth and Planetary Science Letters, 272, 620-626.

Morard, G., Siebert, J., Andrault, D., Guignot, N., Garbarino, G., Guyot, F., and Antonangeli, D. (2013) The Earth's core composition from high pressure density measurements of liquid iron alloys. Earth and Planetary Science Letters, 373, 169-178.

Mori, Y., Ozawa, H., Hirose, K., Sinmyo, R., Shigehiko, T., Morard, G., and Ohishi, Y. (2017) Melting experiments on Fe–Fe_3S system to 254 GPa Earth and Planetary Science Letters, 464, 135-141.

Mouhat, F., and Coudert, F.-X. (2014) Necessary and sufficient elastic stability conditions in various crystal systems. Physical Review B, 90, 224104.

Ono, S., and Kikegawa, T. (2006) High-pressure study of FeS, between 20 and 120 GPa, using synchrotron X-ray powder diffraction. American Mineralogist, 91, 1941-1944.

Ono, S., and Mibe, K. (2010) Magnetic transition of iron carbide at high pressures. Physics of the Earth and Planetary Interiors, 180, 1-6.

Otero-de-la-Rosa, A., Abassi-Perez, D., and Luana, V. (2011) First-principles prediction of crystal structures at high temperatures using the quasiharmonic approximation. Computer Physics Communications, 182, 2232.

Ozawa, H., Hirose, K., Suzuki, T., Ohishi, Y., and Hirao, N. (2013) Decomposition of Fe_3S above 250 GPa. Geophysical Research Letters, 40, 4845-4849.

Perdew, J.P., Burke, K., and Ernzerhof, M. (1996) Generalized gradient approximation made simple. Physical Review Letters, 77, 3865-3868.

Perdew, J.P., Ruzsinszky, A., Csonka, G.I., Vydrov, O.A., Scuseria, G.E., Constantin, X.Z., and Burke, K. (2008) Restoring the density-gradient expansion for exchange in solids and surfaces. Physical Review Letters, 100, 136406.

Pinilla, C., Blanchard, M., Balan, E., Natarajan, S.K., Vuilleiumier, R., and Mauri, F. (2015) Equilibrium magnesium isotope fractionation between aqueous Mg^{2+} and carbonate minerals: Insights from path integral molecular dynamics. Geochimica et Cosmochimica Acta, 163, 126-139.

Pinilla, C., De Moya, A., Blanchard, M., Morard, G., and Roskosz, M. (2020) First principles investigation of equilibrium iron isotope fractionation in FeS alloys at Earth's core formation conditions. In preparation.

Poitrasson, F., Halliday, A.N., Lee, D.-C., Levasseur, S., and Teutsch, N. (2004) Iron isotope differences between Earth, Moon, Mars and Vesta as possible records of contrasted accretion mechanisms. Earth and Planetary Science Letters, 223, 253-266.

Poitrasson, F., Roskosz, M., and Corgne, A. (2009) No iron isotope fractionation between molten alloys and silicate melt to 2000 °C and 7.7 GPa: Experimental evidence and implications for planetary differentiation and accretion. Earth and Planetary Science Letters, 278, 376-385.

Roberts, R.W., and Ruppin, R. (1971) Volume Dependence of the Gruneisen Parameter of Alkali Halides. Physical Review B, 4, 2041-2046.

Seagle, C.T., Campbell, A.J., Heinz, D.L., Shen, G., and Prakapenka, V.B. (2006) Thermal equation of state of Fe_3S and implications for sulfur in Earth ' s core. Journal of Geophysical Research, 111, B06209.

Shahar, A., Hillgren, V.J., Horan, M.F., Mesa-Garcia, J., Kaufman, L.A., and Mock, T.D. (2015) Sulfur-controlled iron isotope fractionation experiments of core formation in planetary bodies. Geochimica et Cosmochimica Acta, 150, 253-264.

Shahar, A., Schauble, E.A., Caracas, R., Gleason, A.E., Reagan, M.M., Xiao, Y., Shu, J., and Mao, W. (2016) Pressure-dependent isotopic composition of iron alloys. Science, 352(6285), 580.

Shen, G., Lin, J., Fei, Y., Mao, H., Hu, M., and Chow, P. (2003) Magnetic and Structural Transition in Fe_3S at High Pressures, American Geophysical Union, Fall Meeting 2003, abstract id.V31D-0961.

Sherman, D.M. (1997) pressure and the composition of the Earth's core: constraints on S and Si vs. temperature. Earth and Planetary Science Letters, 153, 149-155

.

Sohl, F., Schubert, G., and Spohn, T. (2005) Geophysical constraints on the composition and structure of the Martian interior. Journal of Geophysical Research, 110, E12008.

Steentra, E.S., and van Westrenen, W. (2018) A synthesis of geochemical constraints on the inventory of light elements in the core of Mars. Icarus, 315, 69-78.

Tateno, S., Ozawa, H., Hirose, K., Suzuki, T., I-Kawaguchi, S., and Hirao, N. (2019) Fe_2S: The most Fe-Rich Iron Sulfide at the Earth's inner Core Pressure. Geophysical Research Letters.

Taylor, M.B., Barrera, G.D., Allan, N.L., and Barron, T.H.K. (1997) Free energy derivatives and structure optimisation within quasiharmonic lattice dynamics. Physical Review B, 56, 14380-14390.

Taylor, M.B., Barrera, G.D., Allan, N.L., Barron, T.H.K., and Mackrodt, W.C. (1998) SHELL – a code for lattice dynamics and structure optimisation of ionic crystals. Computer Physics Communications, 109, 135-143.

Thompson, S., Komabashi, T., Breton, H., Suehiro, S., Glazyrin, K., Pakhomova, A., and Ohishi, Y. (2020) Compresion experiments to 126 GPa and 2500 K and thermal equation of state of Fe3S: Implications for sulfur in the Earth's core. Earth and Planetary Science Letters, 534, 116080.

Tkalcic, H. (2015) Complex inner core of the Earth: The last frontier of global seismology. Reviews of Geophysics, 53, 59-94.

Togo, A., and Tanaka, I. (2015) First principles phonon calculations in material sciences Scr. Mater., 108, 1-5.

Vocadlo, L., Brodholt, J., Dobson, D.P., Kinight, K.S., Marshall, W.G., and Price, G.D. (2002) The effect of ferromagnetism on the equation of state of Fe_3C studied by first-principles calculations. Earth and Planetary Science Letters, 203, 567-575.

Weyer, S., Anbar, A.D., Brey, G.P., Münker, C., Mezger, K., and Woodland, A.B. (2005) Iron isotope fractionation during planetary differentiation. Earth and Planetary Science Letters, 240, 251-264.

Wicht, J., and Sanchez, S. (2019) Advances in geodynamo modelling. Geophysical & Astrophysical Fluid Dynamics, 113, 2-50.

Wu, X., Mookherjee, M., Gu, T., and Qin, S. (2011) Elasticity and anisotropy of iron-nickel phosphides at high pressure. Geophysical Research Letters, 38, L20301.

Yoder, C.F., Konopliv, A.S., Yuan, D.N., Standish, D.M., and Folkner, W.M. (2003) Fluid core size of mars from detection of the solar size. Science, 300, 299-303.

This is the peer-reviewed, final accepted version for American Mineralogist, published by the Mineralogical Society of America.
The published version is subject to change. Cite as Authors (Year) Title. American Mineralogist, in press.
DOI: https://doi.org/10.2138/am-2021-7268. http://www.minsocam.org/

598

599

600 **Figure Captions**

601 **Figure 1.** Crystal structures of the most stable phases of Fe_3S: a) tetragonal Fe_3P-type structure ($I\bar{4}$)
602 and b) the cubic $AuCu_3$-type structure.

603 **Figure 2.** Total energy (per formula unit) vs. volume for the tetragonal and cubic forms of Fe_3S

604 **Figure 3.** Calculated magnetic moment from spin-unrestricted calculations of the three non-
605 equivalent iron atoms in the $I\bar{4}$ structure at different pressures. The black line is the calculated
606 average.

607 **Figure 4.** Ratio of *c*/*a* as a function of pressure for tetragonal Fe_3S (ferromagnetic below 50 GPa,
608 non-magnetic at larger pressures). The straight lines are guides for the eye.

609 **Figure 5.** Thermal expansion coefficient from spin-restricted calculations as a function of
610 temperature for several pressures over the range 50-250 GPa.

611 **Figure 6.** Volume as a function of pressure for the Fe_3S tetrahedral phase at different isotherms. Full
612 red line and green line correspond to calculations at 300 K and 900 K respectively (ferromagnetic
613 below 50 GPa, non-magnetic at higher pressures). Brown diamonds, purple triangles, and green
614 circles correspond to experimental values taken from Kamada et al. (2014), Chen et al. (2007) and
615 Seagle et al. (2006) respectively.

616 **Figure 7.** Phonon dispersion curves and phonon density of states calculated for tetragonal Fe_3S at
617 zero pressure (spin-unrestricted) and 50 GPa (spin-restricted).
618 **Figure 8.** Grüneisen parameter of tetragonal Fe_3S from spin-restricted calculations as a function of
619 temperature at several pressures over the range 50-250 GPa.

620 **Figure 9.** Temperature dependence of the heat capacity C_p from spin-restricted calculations along the
621 isobars of 50 GPa (green dashed line), 100 GPa (red dashed line), 150 GPa (blue dashed line) and
622 200 GPa (violet dashed line). Solid lines are corresponding values of C_v.

Figure 10. Force constants of iron bonds in tetragonal Fe_3S as a function of pressure. "Fe average" refers to the overall mean force constant. Below 50 GPa results are from spin-unrestricted calculations and from spin-restricted at higher pressures.

Figure 11. Elastic properties for tetragonal Fe_3S as a function of pressure: a) calculated elastic constants. b) the isotropic P-wave and S-wave velocities, red-triangles and black-squares correspond to experimental values reported by Lin et al. 2014. c) Bulk and shear modulus estimated from the calculations. Below 50 GPa results are from spin-unrestricted calculations and from spin-restricted at higher pressures.

Figure 12: Variation of a) compressional and b) shear wave velocities as a function of propagation direction and pressure, from spin-restricted calculations.

Table 1. Calculated thermal equation of state parameters for ferromagnetic tetragonal Fe_3S compared with room temperature experimental values and the calculations of Martin et al. (2004). V_0 is the zero-pressure volume per unit cell.

V_0 (Å^3)	K_0 (GPa)	K'_0	*Method*	*Reference*
377.0	170	2.6	Exp	(Fei et al. 2000)
377.0 (fixed)	156	3.8	Exp	(Seagle et al., 2006)
377.0 (fixed)	134	5.1	Exp	(Chen et al. 2007)
377.0 (fixed)	125	5.1	Exp	(Kamada et al. 2014)
377.0 (fixed)	119	5.6	Exp	(Thompson et al. 2020)
338.3	250	4.6	DFT	(Martin et al. 2004)*
339.0	175	5.1	DFT	This study, static
346.0	166	5.2	DFT	This study, including thermal effects at 300 K**

* The calculations of Martin et al. (2004) are non-magnetic (spin-restricted)

638 ** Values extrapolated from our calculations at 50 GPa – 200 GPa using a 3rd order Birch-
639 Murnaghan equation of state.

640

641

642 **Table 2.** Calculated sound velocity ranges (km s^{-1}) and anisotropic coefficients A (%) of Fe_3S

P(GPa)	V_P	V_{S1}	V_{S2}	A_P	A_S
50	7.95-8.81	4.53-4.60	3.43-4.53	9.82	25.32
150	9.78-10.54	5.34-5.64	4.20-5.34	7.24	25.48
250	10.81-11.67	5.85-6.31	4.63-5.85	7.32	26.66

643

644

645

646

647

648

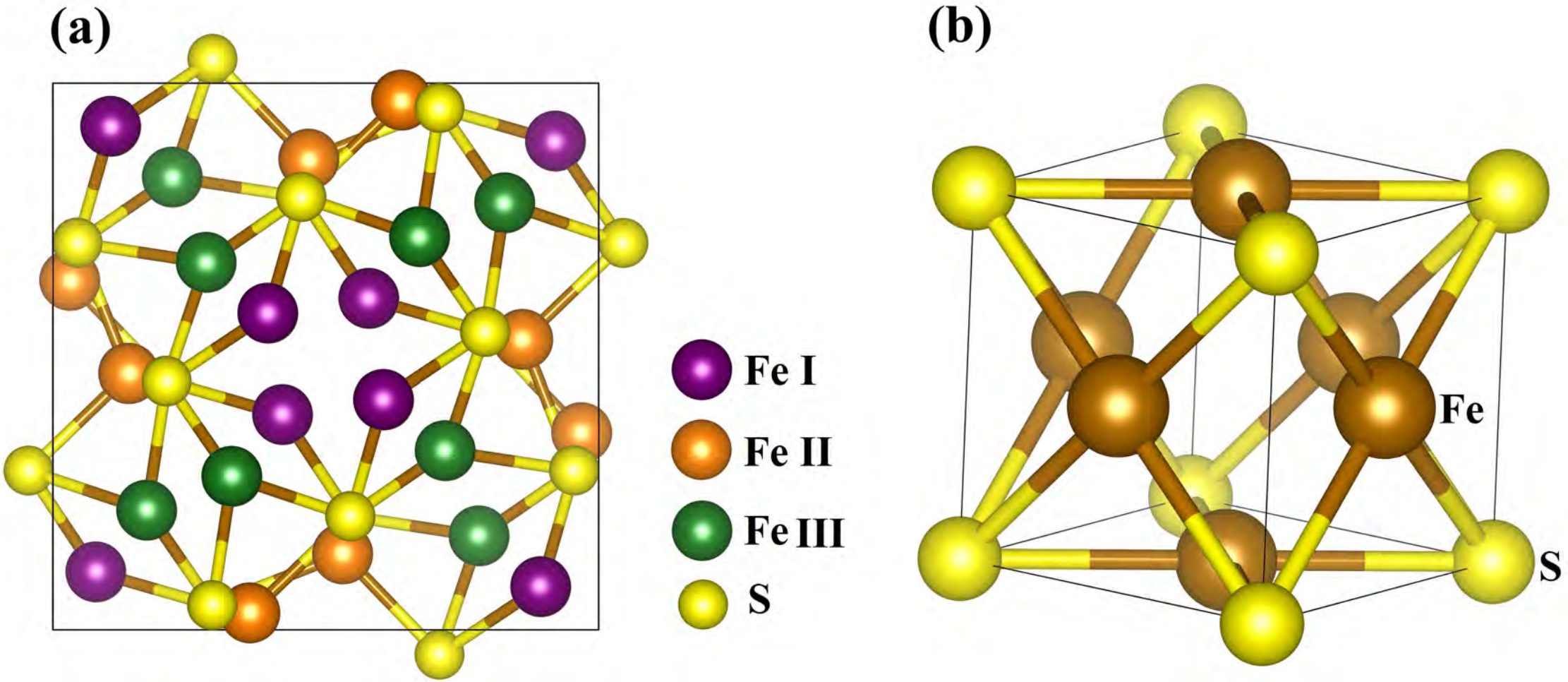

Fig. 1

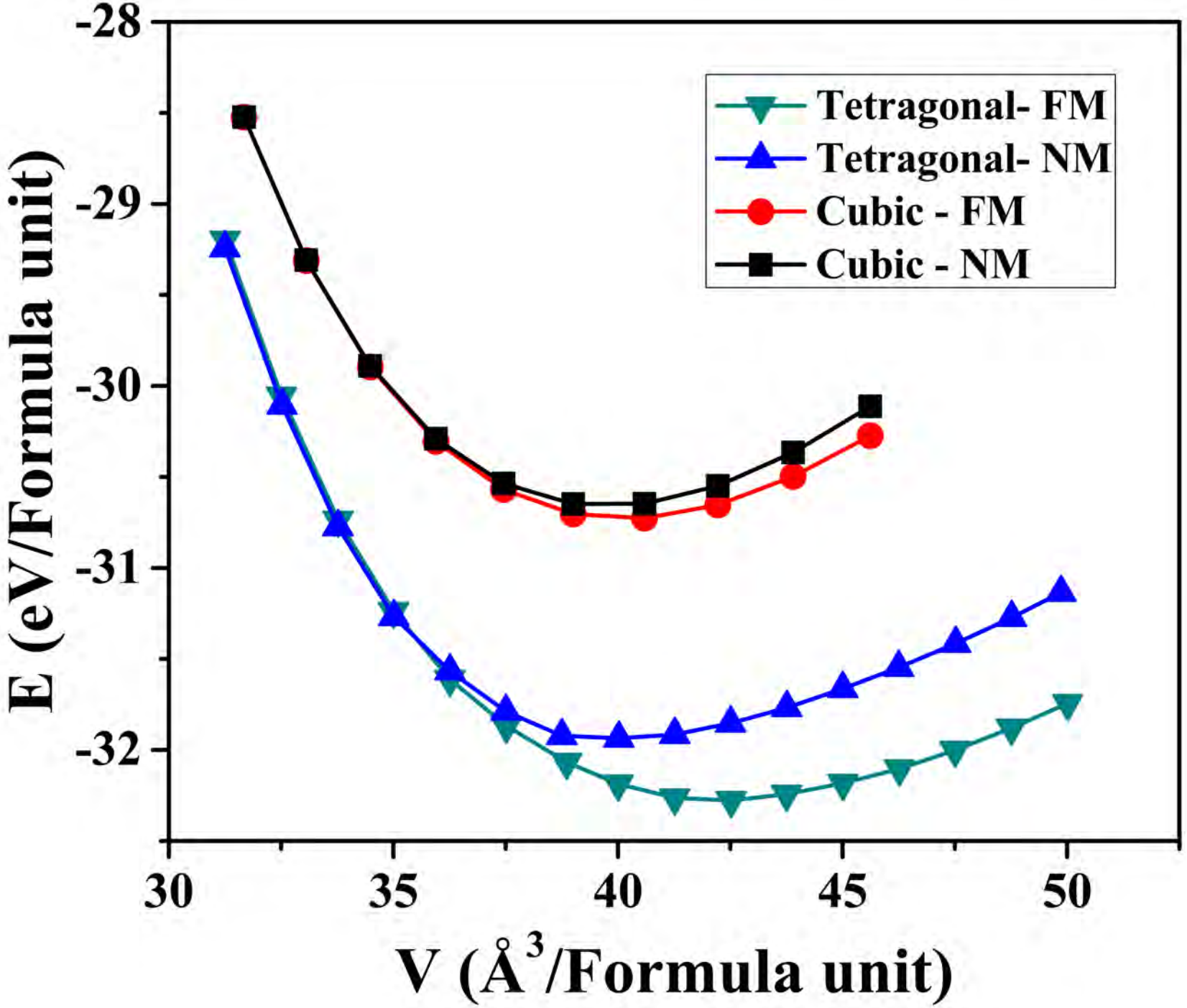
-28
-29
-30
-31
-32
E (eV/Formula unit)
30
35
40
45
50
V (Å^3/Formula unit)
Tetragonal- FM
Tetragonal- NM
Cubic - FM
Cubic - NM

Fig. 2

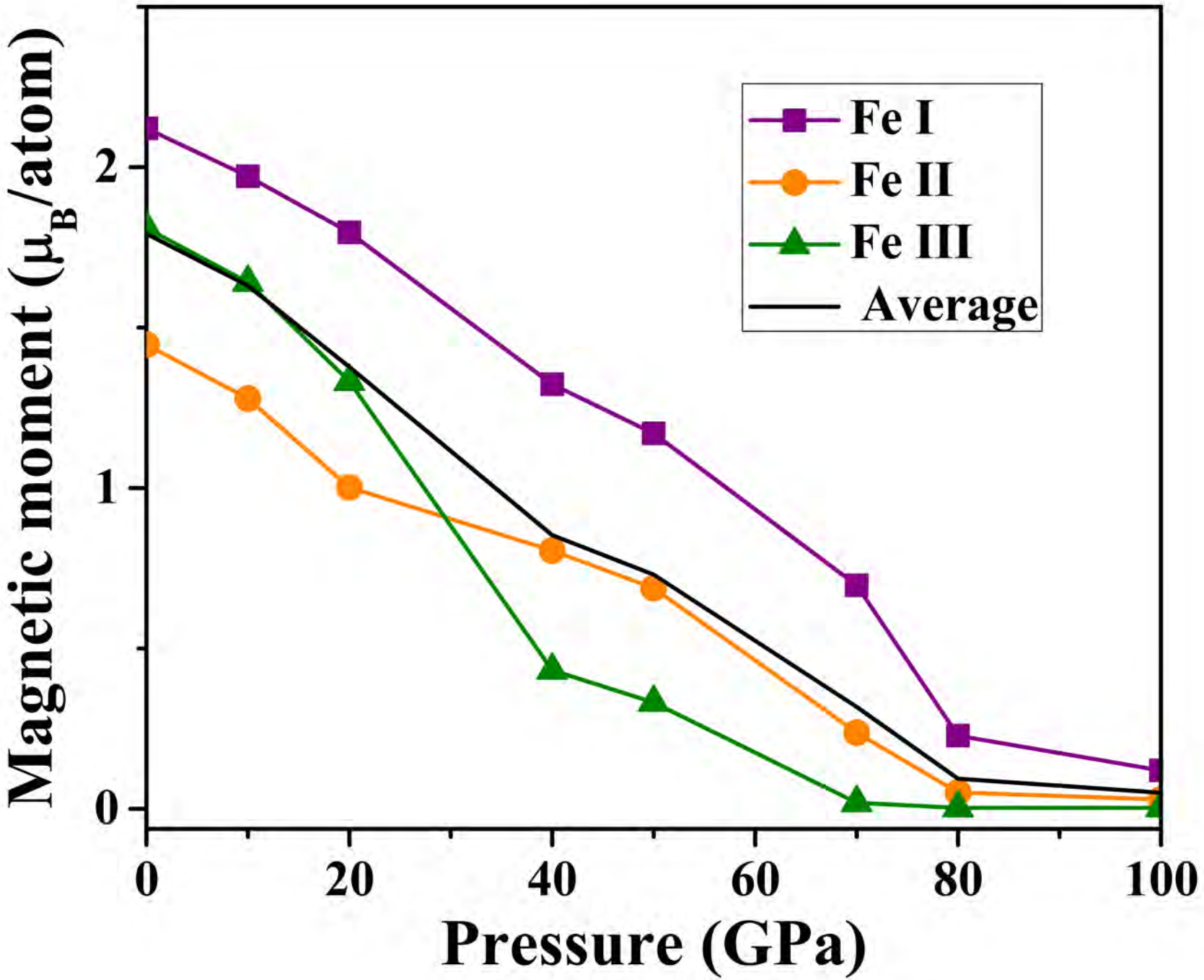
Magnetic moment (μ_B/atom)
Pressure (GPa)
Fe I
Fe II
Fe III
Average
0
1
2
0
20
40
60
80
100

Fig. 3

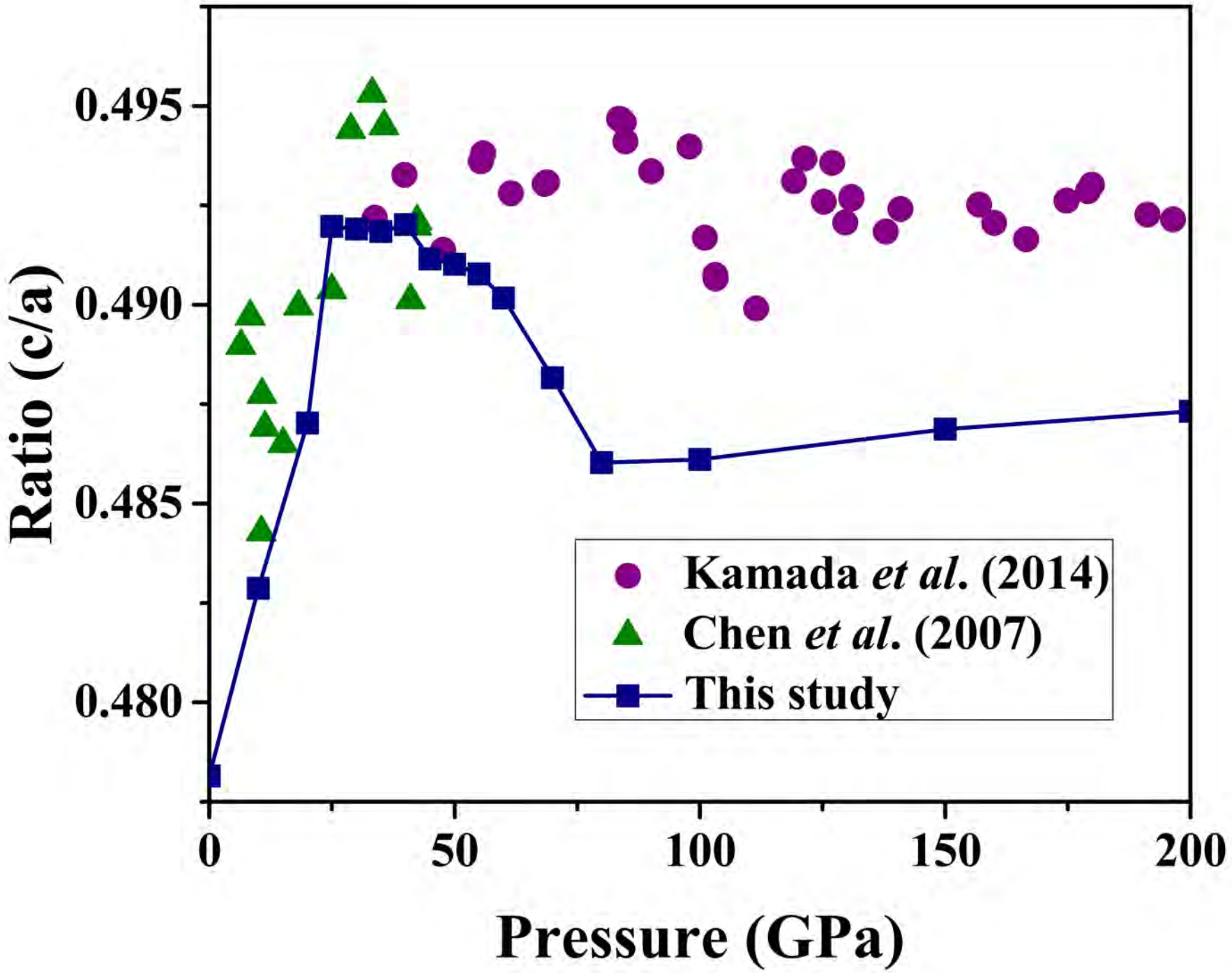
0.495
0.490
0.485
0.480
Ratio (c/a)
0
50
100
150
200
Pressure (GPa)
Kamada et al. (2014)
Chen et al. (2007)
This study

Fig.4

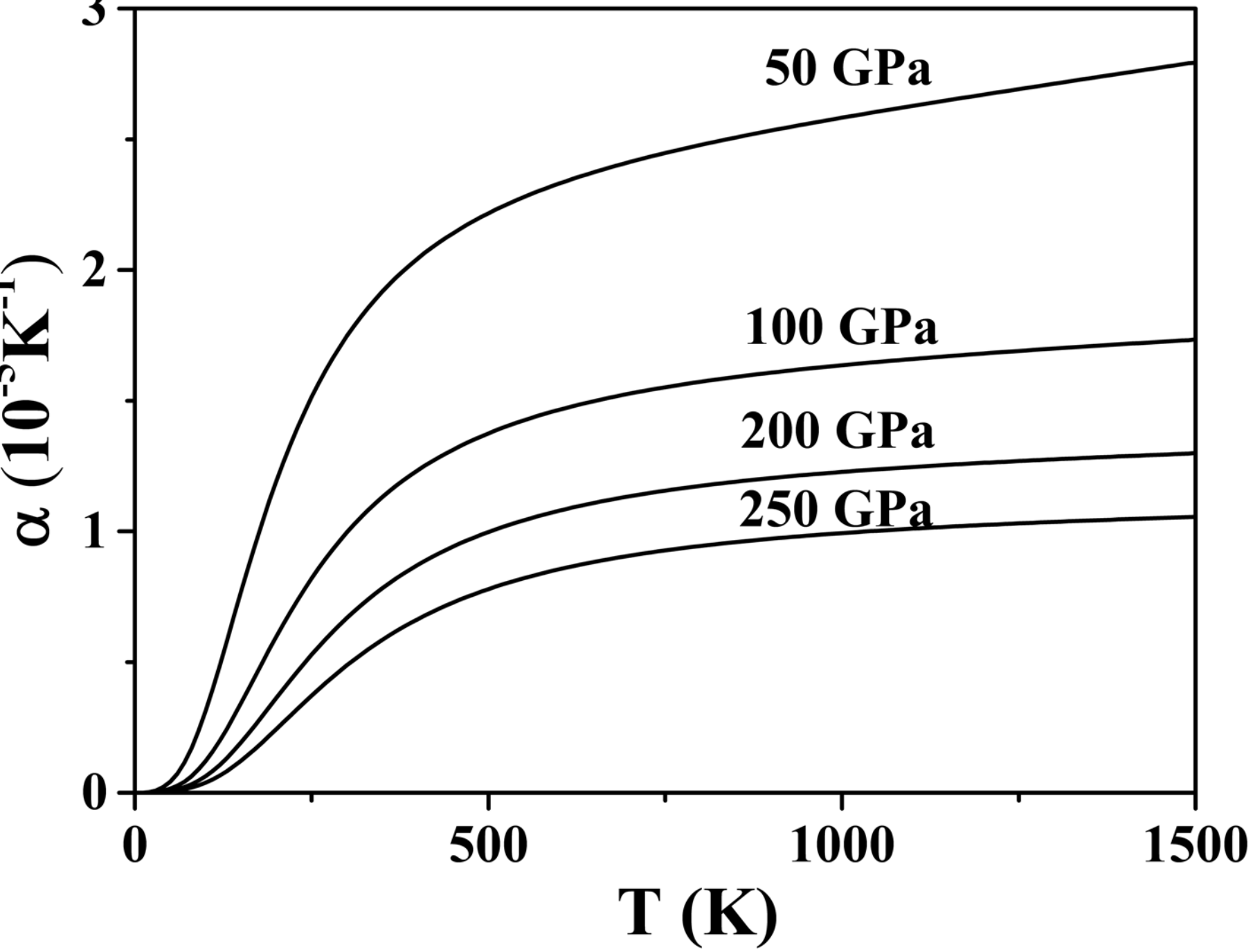

Fig. 5

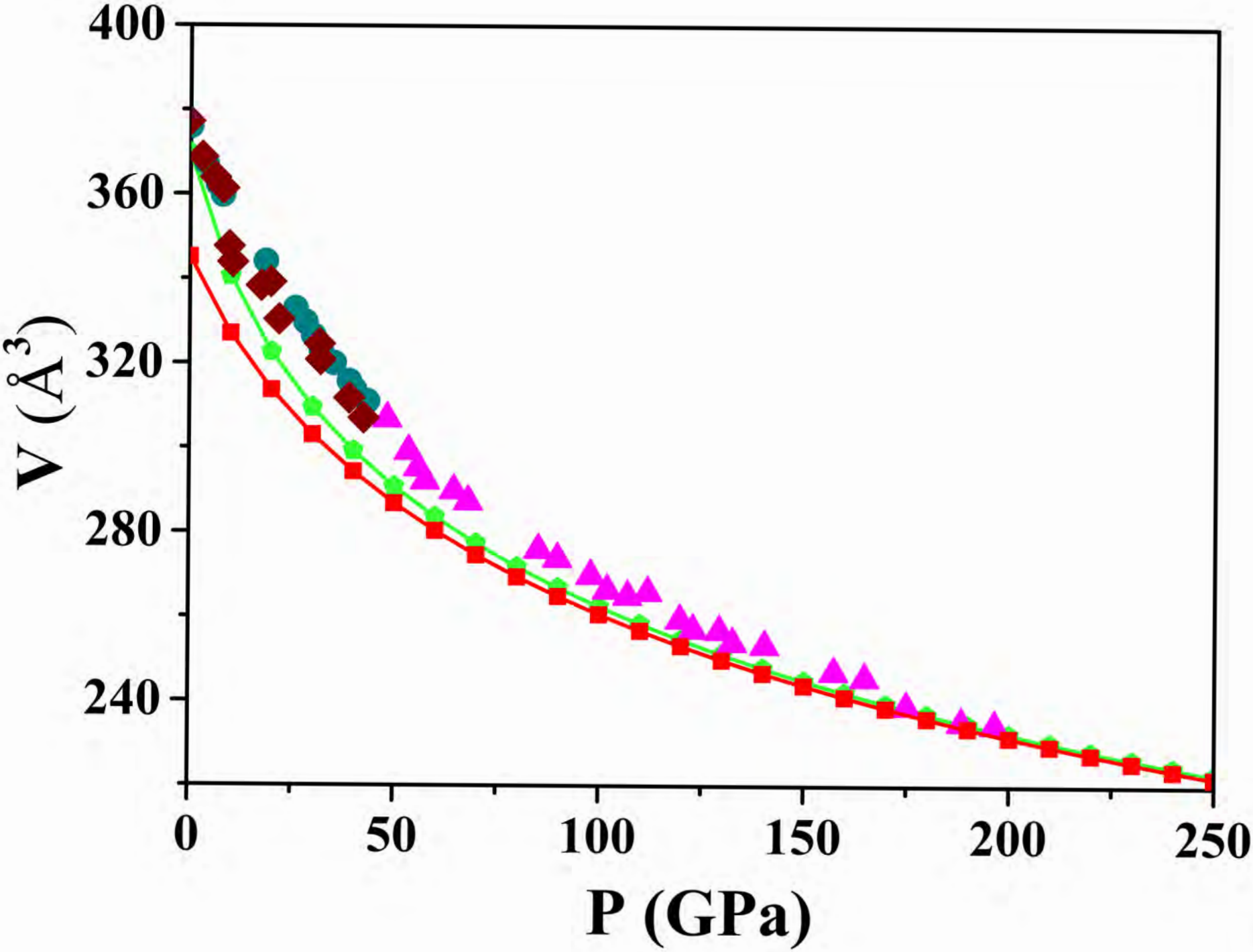

Fig. 6

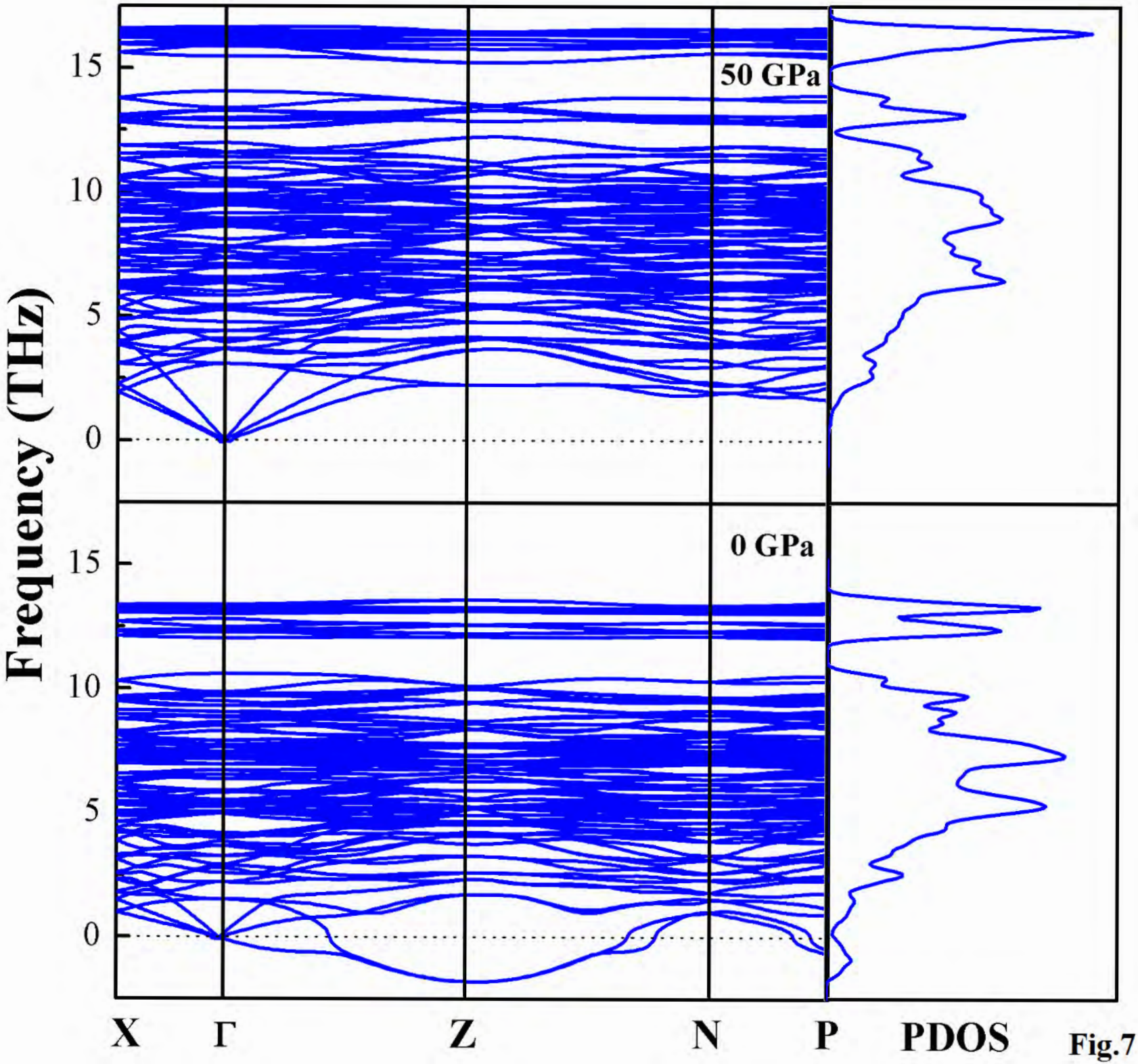

Fig.7

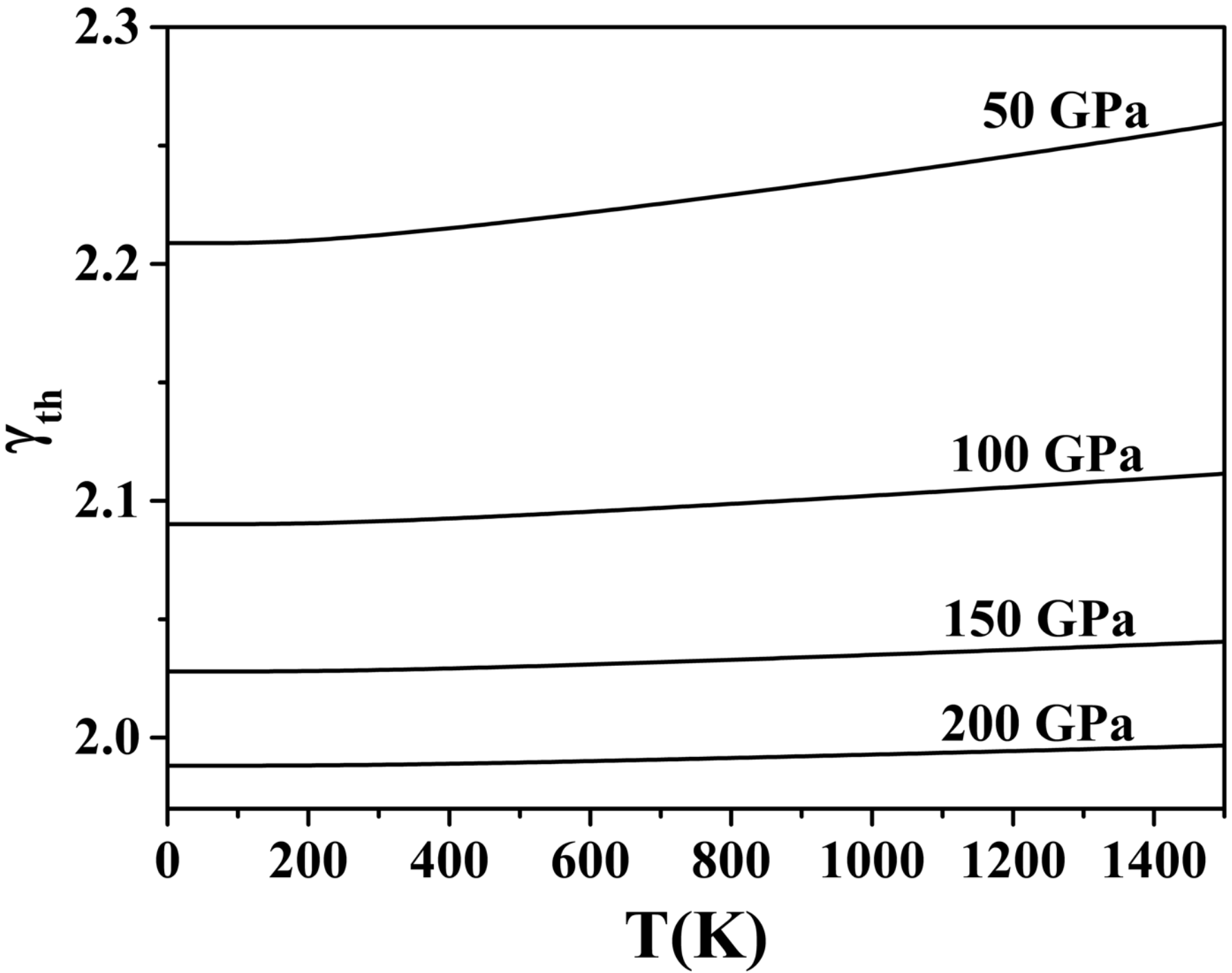
2.3
2.2
2.1
2.0
γ_{th}
50 GPa
100 GPa
150 GPa
200 GPa
0
200
400
600
800
1000
1200
1400
T(K)

Fig.8

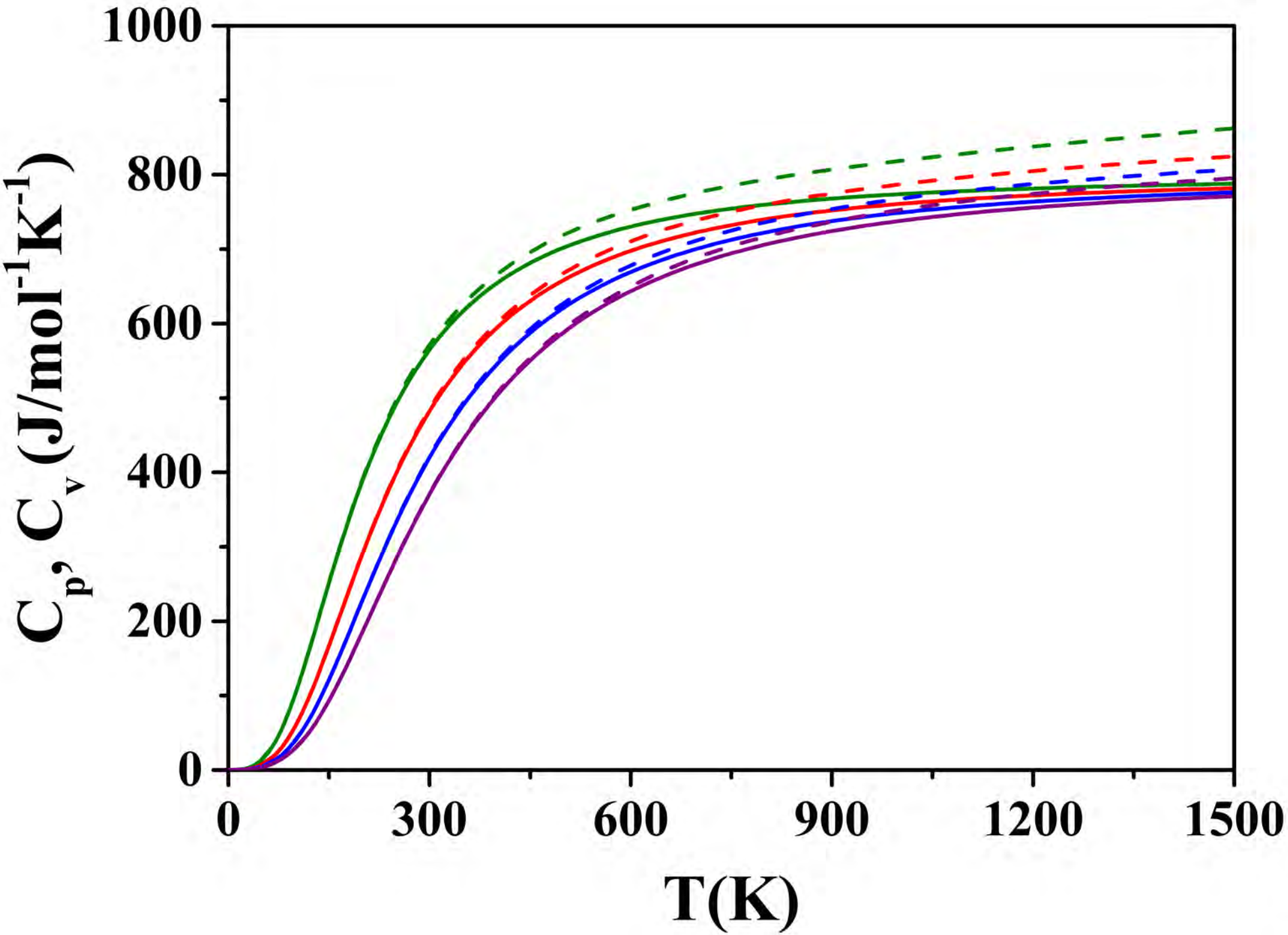

Fig. 9

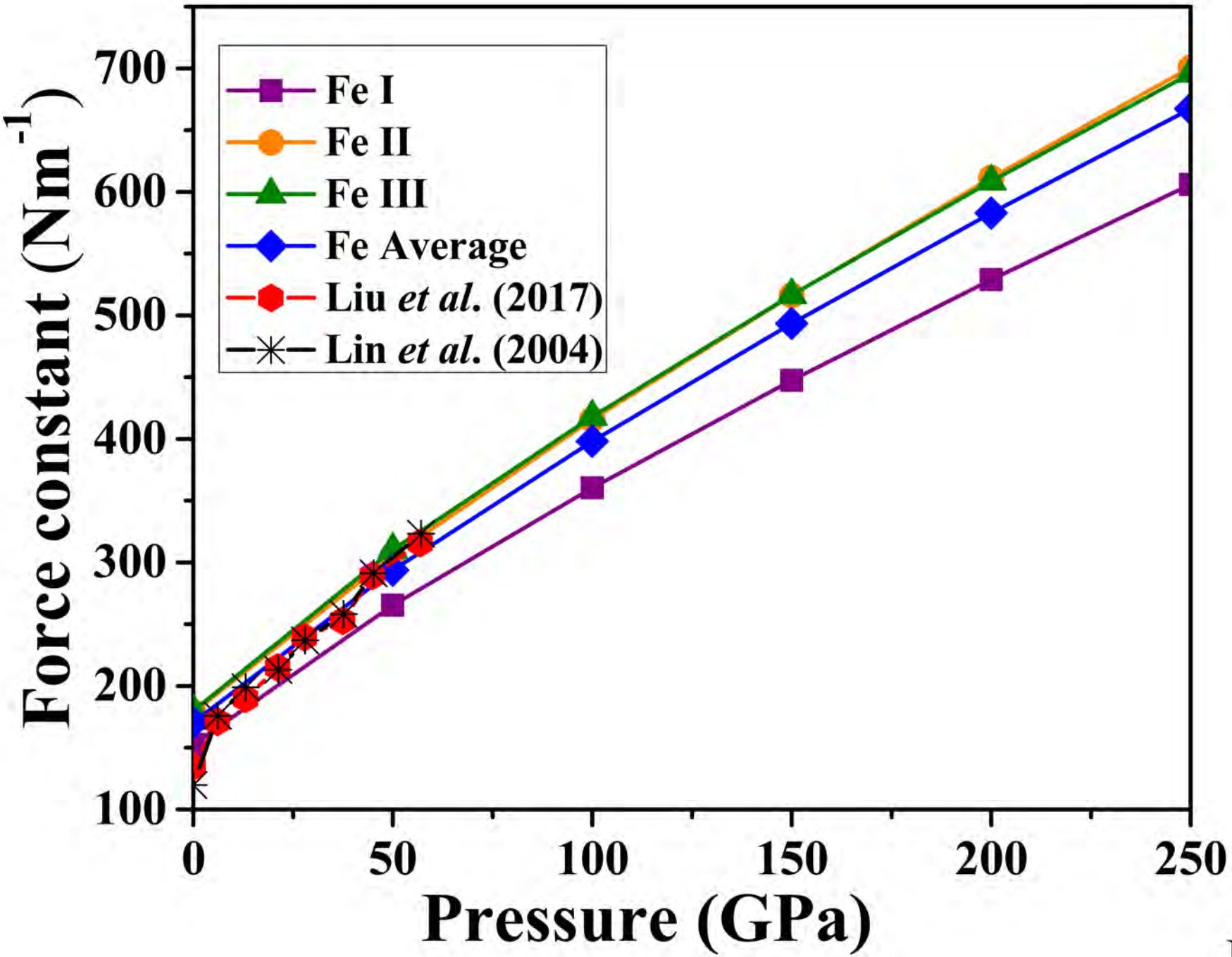
Force constant (Nm^{-1})
Pressure (GPa)
Fe I
Fe II
Fe III
Fe Average
Liu *et al.* (2017)
Lin *et al.* (2004)
100
200
300
400
500
600
700
0
50
100
150
200
250

Fig. 10

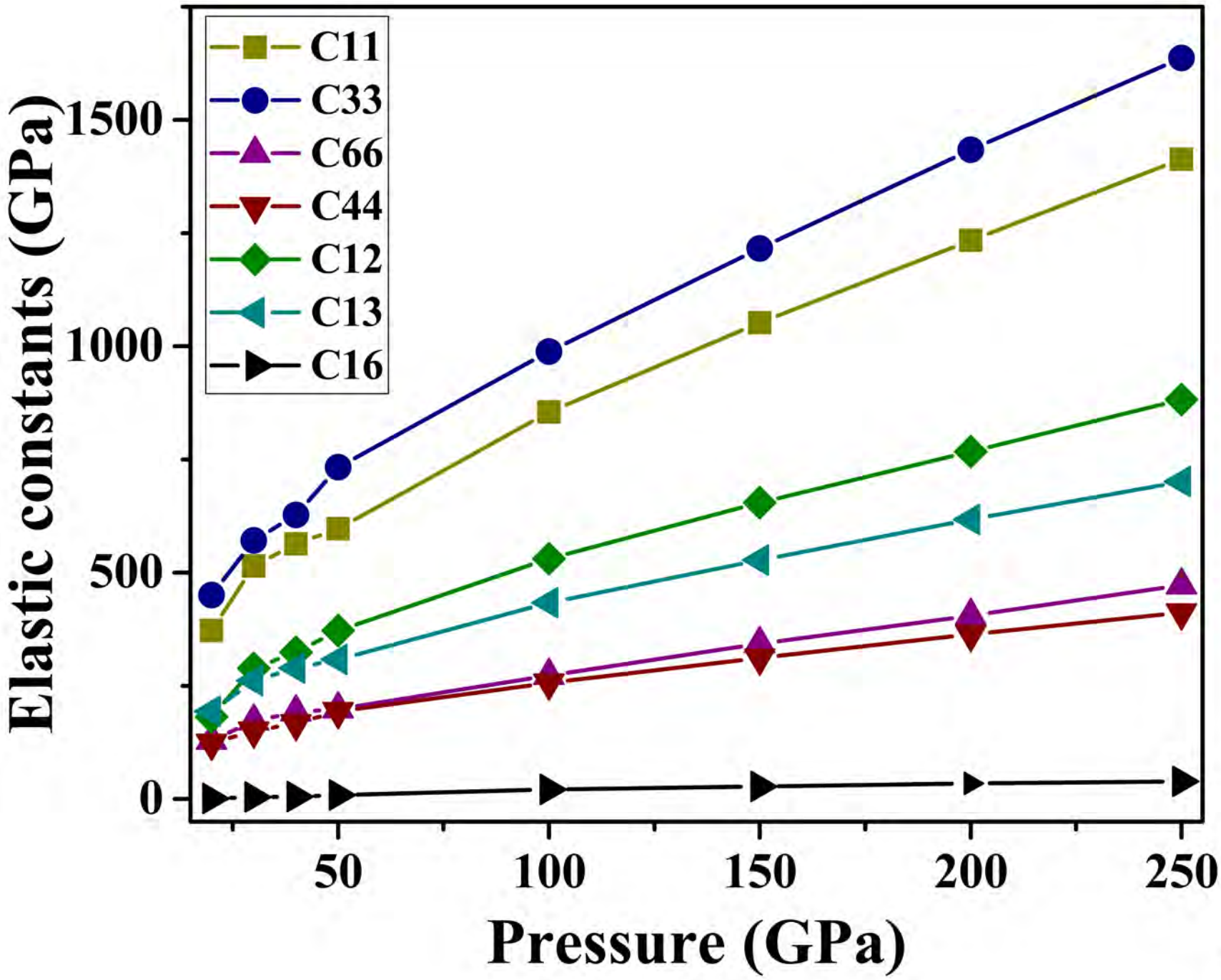
C11
C33
C66
C44
C12
C13
C16
Elastic constants (GPa)
0
500
1000
1500
50
100
150
200
250
Pressure (GPa)

Fig. 11a

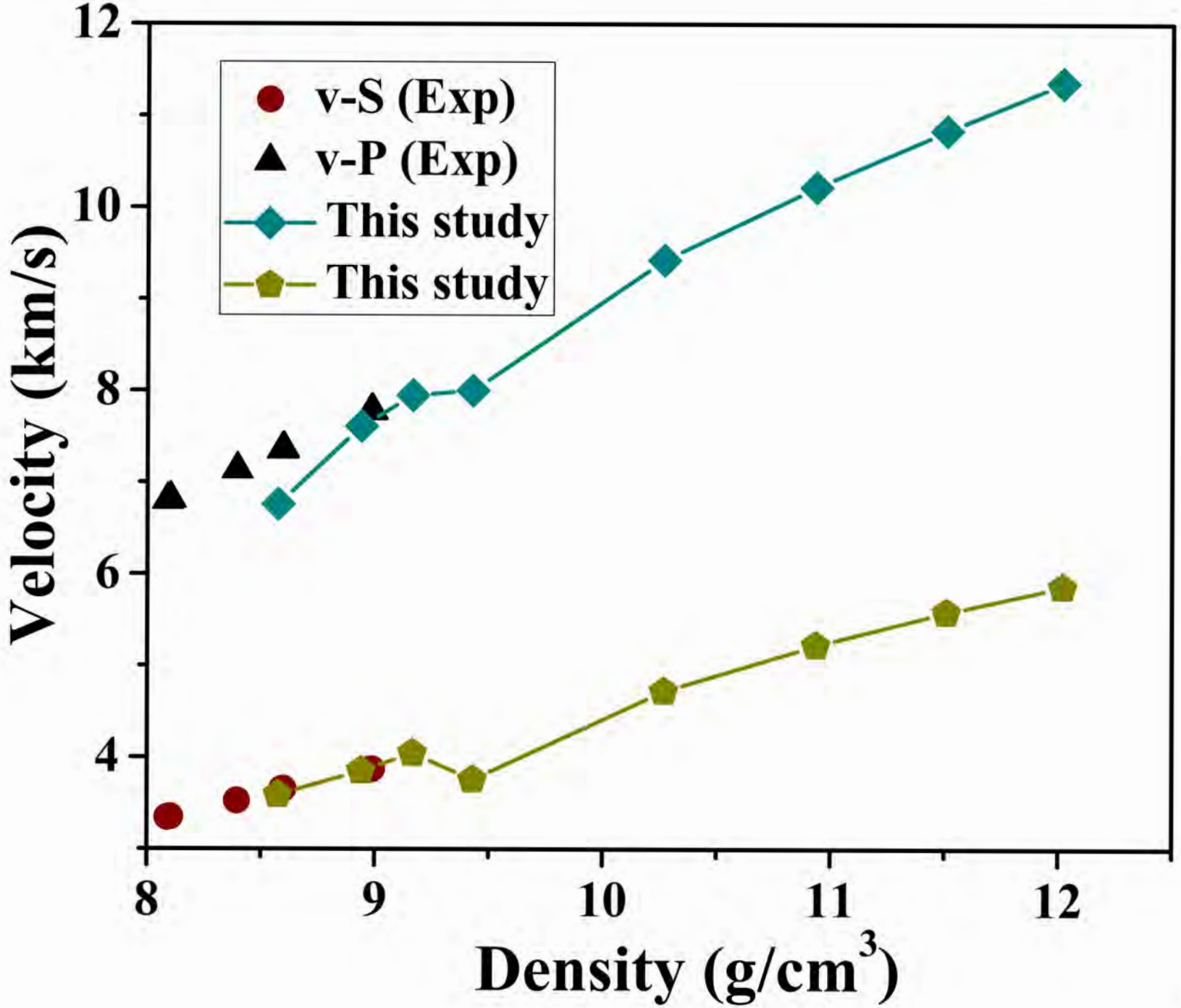
v-S (Exp)
v-P (Exp)
This study
This study
Velocity (km/s)
Density (g/cm3)
12
10
8
6
4
8
9
10
11
12

Fig. 11b

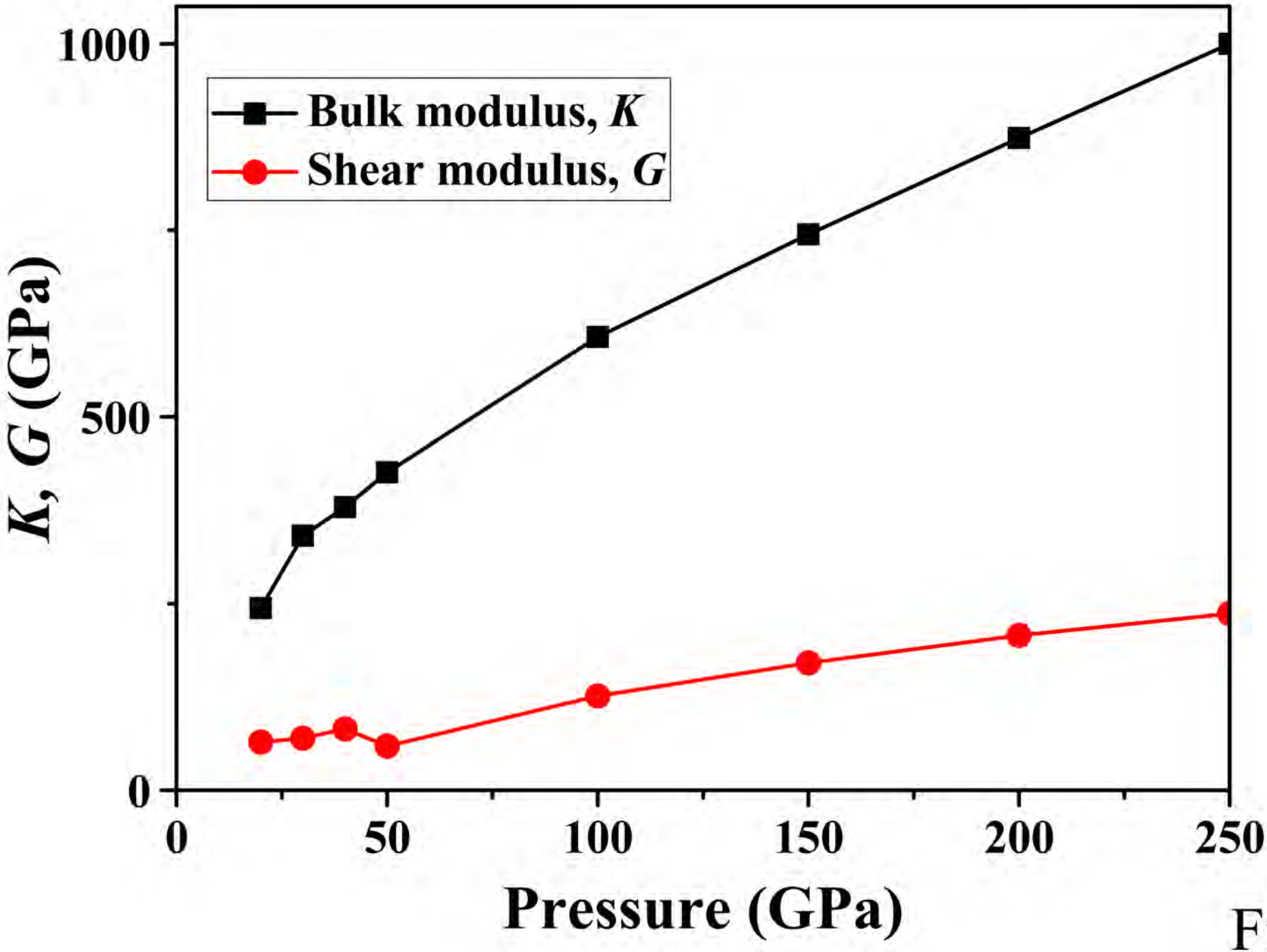
1000
500
0
0
50
100
150
200
250
K, G (GPa)
Pressure (GPa)
Bulk modulus, K
Shear modulus, G

Fig. 11c

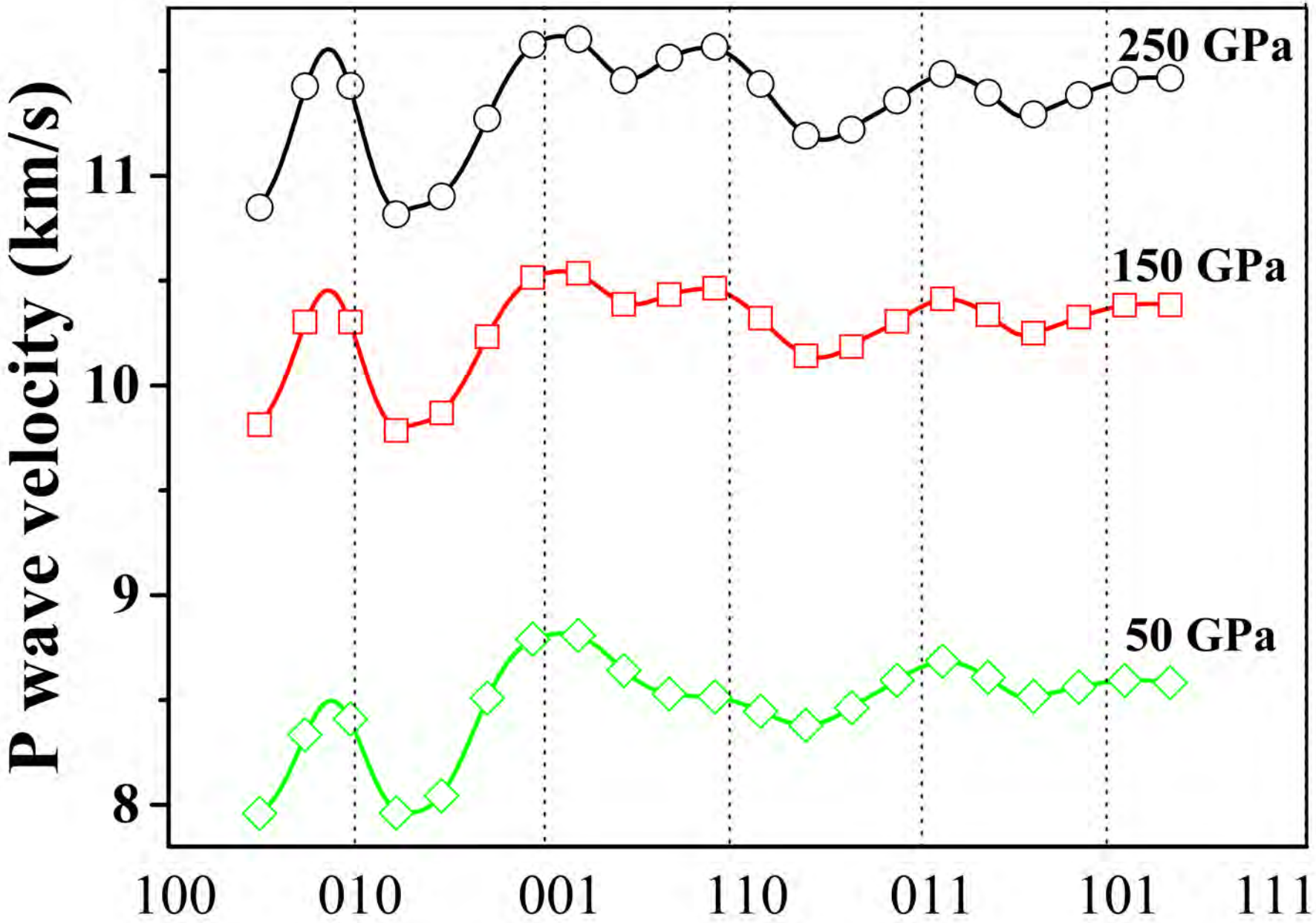
P wave velocity (km/s)
11
10
9
8
250 GPa
150 GPa
50 GPa
100
010
001
110
011
101
111

Fig. 12a

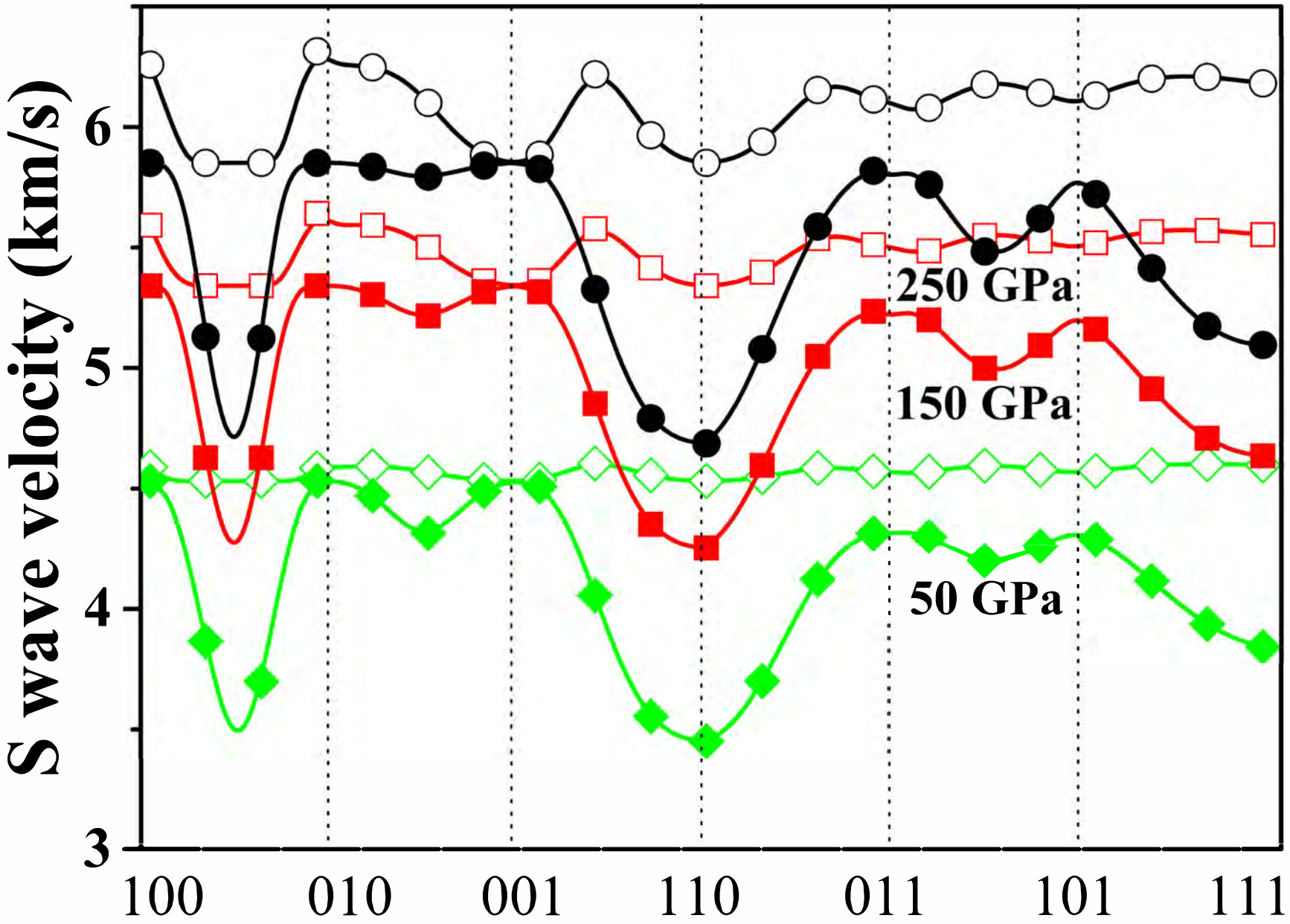
S wave velocity (km/s)
6
5
4
3
250 GPa
150 GPa
50 GPa
100
010
001
110
011
101
111

Fig. 12b